CHEMICAL REVIEWS

Review

pubs.acs.org/CR

# Titanium Dioxide Nanomaterials: Self-Structural Modifications

Lei Liu*[,†] and Xiaobo Chen*[,‡]

[†]State Key Laboratory of Luminescence and Applications, Changchun Institute of Optics, Fine Mechanics and Physics, Chinese Academy of Sciences, 130033, Changchun, Jilin, People's Republic of China

[‡]Department of Chemistry, University of Missouri—Kansas City, Kansas City, Missouri 64110, United States

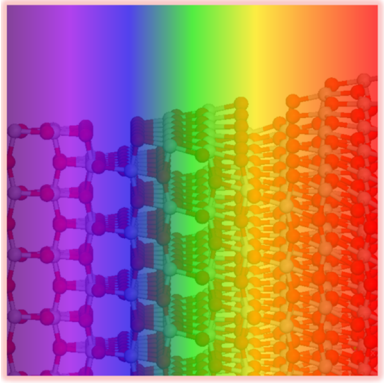

## CONTENTS

1. Introduction 9890
2. Structure Information of $TiO_2$ 9891
3. Self-Structural Modifications in Pure Phases 9892
   3.1. Surface Effects 9892
   3.2. Lattice Strain Effects 9894
   3.3. Nanoscale Effects 9894
4. Self-Structural Modifications in Mixed Phases 9898
   4.1. Improved Photocatalytic Performance 9898
   4.2. Synergistic Effects 9898
   4.3. Interfacial Structural Properties 9899
5. Self-Structural Modifications in Amorphous/Disordered Phases 9900
6. Self-Structural Modifications in Hydrogenated Phases 9901
   6.1. Research Progress in Applications 9901
      6.1.1. Photocatalysis 9901
      6.1.2. Lithium-Ion Battery 9902
      6.1.3. Supercapacitor 9904
      6.1.4. Fuel Cell 9904
      6.1.5. Field Emission 9904
      6.1.6. Microwave Absorption 9904
   6.2. Debates on the Fundamental Properties 9906
      6.2.1. Structural Disorder 9906
      6.2.2. $Ti^{3+}$ 9906
      6.2.3. Ti–H 9907
      6.2.4. Ti–OH 9907
      6.2.5. Oxygen Vacancy 9908
      6.2.6. Valence-Band Edge 9910
      6.2.7. Stability 9910
      6.2.8. Theoretical Models 9911
7. Consideration of Elementary Defects in Self-Structural Modifications 9912
   7.1. Experimental Results 9912
   7.2. Theoretical Analysis 9912
8. Summary 9913
Author Information 9914
   Corresponding Authors 9914
   Notes 9914
   Biographies 9914
Acknowledgments 9914
References 9914

## 1. INTRODUCTION

Titanium dioxide ($TiO_2$), white color, with a high brightness and refractive index, has been widely used as a white pigment since its commercial production in the 1920s.[1] Its low cost, inertness, and nontoxicity make it a particularly good ingredient for paints, ointments,[2] food coloring,[3] sunscreens,[4,5] and many other commercial products.[6] Since the study of the ultraviolet (UV) light-induced photoelectrochemical water splitting on its surfaces in 1972,[7] it has been extensively investigated for various applications. These applications include photocatalytic hydrogen production from water[7−16] or organic chemicals,[17] decomposition[18] and synthesis[19] of organic chemicals, removal of pollutants from the environment,[7−10,20−25] fuel generation from $CO_2$ reduction,[26−40] oxidation of CO,[41] and uses in dye-sensitized solar cells,[42−45] rechargeable batteries/supercapacitors,[46−52] sensors, and biomedical devices.[53−58] Its performance in such applications depends largely on its optical, electronic, structural, morphological, and surface properties as well as on its size, crystallinity, and surface facets.[9,13,14] Great effort has been devoted to adjust these properties in order to improve in its performance. Steady and apparent progress has been seen in the synthesis of its 0-, 1-, 2-, and 3-dimensional nanomaterials and surface facet-selective nano/microstructures as well as in the understanding of its structural, mechanical, thermodynamic, optical, electronic, surface, and interfacial properties.[9,13,14,59] However, its white color and large band-gap limit its practical applications in photocatalytic hydrogen generation, $CO_2$ reduction, and environmental pollution removal.[57,60−69]

Great effort has been devoted to tuning $TiO_2$'s electronic and optical properties from a variety of angles in order to reach a high photoactivity during the last few decades.[57,60−71] Adding noble metals such as Pt or Rh to $TiO_2$ enhanced its photocatalytic reactivity by improving the charge separation efficiency.[70] Heterojunctions with other semiconductors were also used for this purpose.[9,13,14,72] For example, coupling $TiO_2$ with a wide-gap semiconductor like $SnO_2$ was observed in

Special Issue: 2014 Titanium Dioxide Nanomaterials

Received: October 31, 2013
Published: June 23, 2014

Table 1. Structural Parameters of Common $TiO_2$ Phases[134]

| cryst form | cryst syst | space group | density (g/cm$^3$) | unit cell parameters | | | | ref |
|---|---|---|---|---|---|---|---|---|
| | | | | $a$/nm | $b$/nm | $c$/nm | $\beta$/deg | |
| anatase | tetragonal | $I4_1/amd$ | 3.83 | 0.379 | | 0.951 | | 136 |
| rutile | tetragonal | $P4_2/mnm$ | 4.24 | 0.459 | | 0.296 | | 136 |
| brookite | orthorhombic | $Pbca$ | 0.17 | 0.918 | 0.545 | 0.515 | | 137 |
| $TiO_2$(B) | monoclinic | $Pbca$ | 3.64 | 1.216 | 0.374 | 0.651 | 107.3 | 132 |

enhancing the charge separation and thus the photocatalytic activity,[73,74] addition of small-gap semiconductors as light sensitizers helped $TiO_2$ with more solar absorption in the visible region,[13,14,72] and the CdS/$TiO_2$ heterogeneous system displayed enhanced visible-light activity in methylene blue decomposition,[9,13] nitric oxidation in air,[75] and hydrogen production from water;[76] when sensitized with ruthenium dye complexes, a solar conversion efficiency as high as 10−11% was successfully demonstrated.[77−79] Introducing dopants or defects into the $TiO_2$ matrix was used to enhance its solar utilization.[80] Metal ions, if doped chemically at suitable amounts, enhanced the photoactivity of $TiO_2$ significantly,[60] despite a concern of the thermal instability due to the increase of charge-recombination centers induced by the localized d states of the metal ions within the band gap.[60] Nonmetal elements, if doped under the right conditions, induced the effective band-gap narrowing of $TiO_2$ and improved its visible-light photoactivity.[64] Nitrogen, carbon, sulfur, and iodine were used as examples to reduce the band gap of $TiO_2$.[64,65,81−84] Metal and nonmetal elements, when codoped, were recently used for enhancing water-splitting hydrogen generation through better visible-light response.[85−97] Such enhancements were observed on systems including (Mo, C),[85−90] (Mo, N),[91] (Fe, N),[92−94] (Ta,N),[95] (Ni, N),[96] and (W,C) codoped $TiO_2$.[97] In such doping efforts usually it is the alien atoms or compounds that bring the electronic states into the band gap of $TiO_2$ and make it eventually able to absorb visible solar energy.

In addition, visible-light activity can be triggered by intrinsic defects as well, such as oxygen vacancy ($V_O$).[98,99] Electrons trapped in oxygen vacancies were detected under visible-light irradiation in $TiO_2$ after hydrogen-plasma treatment.[98] The $V_O$ states, located within the band gap, contributed to the visible-light activity in NO,[98,100] 2-propanol, and benzoic acid removal.[101] Hydrogen thermal treatment of $TiO_2$ nanocrystals was demonstrated as a conceptually new way of enhancing solar absorption in the visible-light and near-infrared regions.[102−104] This treatment led to formation of black $TiO_2$ nanoparticles which contained structural disorders near the surface.[102−104] Such black $TiO_2$ nanoparticles displayed excellent photoactivity and stability in photocatalytic hydrogen generation.[102] This approach was consequently suggested as a general concept of self-structural modification and suggested as a new direction in modifying the optical and electrical properties in nanostructured semiconductors.[103] Besides, modification of the structural factors of $TiO_2$,[105] including the phase,[106] morphology,[107−110] structure,[111−113] and porosity,[114,115] has been shown to affect its photochemical activity. For example, the mixed anatase/rutile phase of $TiO_2$ was well known to possess higher photoactivity than either pure phase.[105,116,117] Degussa P25, the currently widely used mixed-phase material (containing anatase/rutile/amorphous),[118] exhibited enhanced photocatalytic and photovoltaic performance from both theoretical[119] and experimental[120] studies, which was believed to benefit from the synergistic effects between the phases.[121,122] The electronic properties of nanomaterials with a high surface-to-bulk ratio were especially sensitive to their structural morphologies.[123,124] The surface morphology of nanocrystalline semiconductors can generally result in an increased chemical activity, lowered melting point, increased phase-transition pressure, and higher solubility, for instance, when compared to their bulk counterparts.[123−125]

We noticed there have been many excellent reviews on $TiO_2$ and its nanomaterials in past years and decades.[8−10,20−23,46,126−128] Here, we aim to summarize the aforementioned efforts in the structural modifications of $TiO_2$ without introduction of any alien elements or compounds or any other species besides the normal valence states of $Ti^{4+}$ and $O^{2-}$ in $TiO_2$. Therefore, we refer to these variations in structure to "self-structural modification" throughout this review. We mainly summarize the electronic and optical property changes induced by such self-structural modifications as they play a most important role in its applications. We intend to provide an overview of the functional properties of $TiO_2$ enhanced by structural morphology and describe the proposed mechanisms of the relevant processes. We briefly review the self-structural modifications on pure-phase $TiO_2$ first and then on mixed phases, amorphous/disorder phases, hydrogenated phases, and finally on $Ti^{3+}$ and $V_O$ aspects which may have been brought up in these self-structural modifications. We would like to point out that this review will be somehow knowledgeably biased, as we realize that we will certainly overlook some of the important literatures, although we try our best to cover all related research efforts and findings. The biases may also come from the limited knowledge and time of the authors in preparing this review and more importantly the rapid developments in this field. Nevertheless, we sincerely hope this review will stimulate new ideas and discoveries to advance progress in the fundamental studies and applied research of $TiO_2$ nanomaterials.

## 2. STRUCTURE INFORMATION OF $TIO_2$

$TiO_2$ is commonly seen in four crystalline polymorphs: tetragonal rutile, tetragonal anatase, orthorhombic brookite, and monoclinic $TiO_2$(B).[129−132] Among them, rutile is more easily obtained at higher temperatures, and the others are more easily obtained at lower temperatures, and $TiO_2$(B) is the least dense polymorph.[132−134] Table 1 lists their structural parameters.[134] In addition, other less common phases have been reported as well.[131,135]

In this review, we shall focus on the most widely studied phases of $TiO_2$: anatase and rutile. They have a common primary structural unit, the $TiO_6$ octahedron, as shown in Figure 1.[127,138,139] The octahedron in both phases is slightly distorted from the perfect octahedron. The bond length in the apical directions is slightly larger than that in the equatorial directions.[127] The bond lengths also differ between these two phases. The Ti−O bond lengths are 1.937 and 1.966 Å for anatase and 1.946 and 1.983 Å for rutile in the equatorial and


dx.doi.org/10.1021/cr400624r | Chem. Rev. 2014, 114, 9890−9918

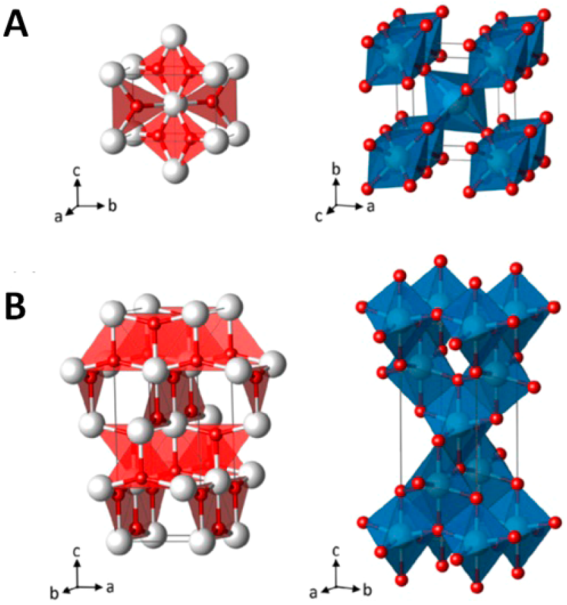


**Figure 1.** Polyhedral representation of the rutile (a) and anatase (b) structures.[140] (Reprinted with permission from ref 140. Copyright 2012 IOP Publishing Ltd.)

apical directions, respectively.[127] The structural difference of these two phases is caused by the different stacking arrangements of their octahedra. In anatase, four of the eight neighbors of each octahedron share edges and the others share corners. The corner-sharing octahedron forms (001) planes and is connected to their edges with the plane of octahedra below.[127] In rutile, each octahedron has 10 neighbors: two share edges, and eight share corners. The neighbors share corners along the [110]-type direction and are stacked with their long axis alternating by 90°.[127] The different structural arrangements result in different space groups: $D_{4h}^{19}$-$I4_1/amd$ for anatase and $D_{4h}^{14}$-$P4_2/mnm$ for rutile.[127,138,139] Similarly, other phases of $TiO_2$ have different Ti−O bond strengths and stacking of the $TiO_6$ octahedra and corresponding space groups. However, it is not clear if the bond length difference causes the different stacking of the $TiO_6$ octahedra or the opposite. Seeing as both the bond length and the stacking are different for these two phases, the Ti−O bond strength and bond coupling are expected to be different, as are their physical and chemical/photochemical properties.

Bulk anatase and rutile have band gaps of 3.2 (387 nm) and 3.0 eV (413 nm), respectively.[131] The difference in the band gap and absorption onset is naturally attributed to the crystal structure difference in the lattice (including both the bond length and the $TiO_6$ stacking), which causes different orbital coupling between the oxygen 2p and titanium 3d orbitals.[9] The band-gap difference seems very straightforward at first glance when we consider the more diverse Ti−O bond lengths of rutile than those of anatase.

The coexistence of the various phases of $TiO_2$ suggests that one of them has the minimal Gibbs free energy, while the others have subminimal ones.[141] Anatase phase is more commonly seen for particles synthesized at room temperature and rutile at high temperatures.[141] The energy barrier for the structural transformation between these two phases was estimated from their phase-transformation temperature.[141,142] This temperature was shown to be size dependent, seeing that the surface area increases rapidly with a decrease of particle size and surfaces are normally full of unsaturated atoms with many dangling bonds.[142,143] Surface relaxation and reconstruction has been frequently reported with Ti−O bond length and bond order distortions.[127] These distortions in many cases caused a thin layer of disordered phase with lattice parameters different from the bulk phase or any other phases.[127,144] Further distortions led to the "coarser" surface of one phase with parameters much closer toward the other,[144] as both phases share the same $TiO_6$ octahedra and the difference of Ti−O bond lengths is small. This eventually led to the incubation and transition into a new phase.[144,145] The anatase−rutile interfaces were believed to be somehow disordered in a narrow region at the interface,[144,145] and structural rearrangements from the anatase side were suggested to cause the rutile octahedral structural formation at the interface.[144]

## 3. SELF-STRUCTURAL MODIFICATIONS IN PURE PHASES

### 3.1. Surface Effects

Truncated from the chemically stoichiometric bulk, the atoms on the surface are normally not saturated and have many dangling bonds.[123] One effect of these unsaturated bonds is that they cause high surface activities to react with adjacent molecules or particles to form new compounds.[123,124,127,146,147] Another prominent effect is that they introduce electronic states in the band gap, causing long-tail optical absorption and red-shifted optical emission.[9,127] The surface effects mainly refer to the electronic and optical effects caused by the bonding structural changes on the surface. Changing the surface area or structural porosity is possible to bring the surface effects here if such bonding structural changes exist in these structures. The Ti−O bonds on the surface have different parameters from the bulk after relaxation and reconstruction (Figure 2).[127] Thus,

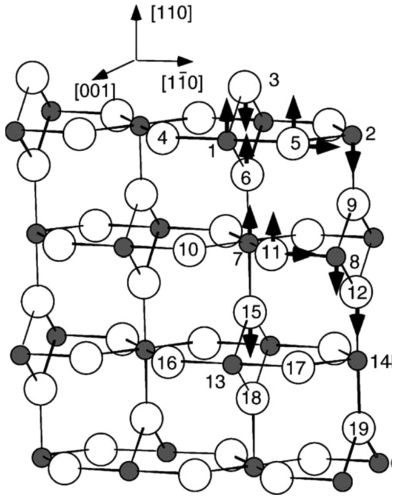


**Figure 2.** Model of the $TiO_2$ (110)−(1 × 1) surface. Relaxations of surface atoms are indicated.[127,149] (Reprinted with permission from ref 127. Copyright 2003 Elsevier Science B.V.)

different truncated facets of $TiO_2$ crystals display distinctly different electronic behaviors from each other and from the bulk due to their different bonding structures and self-structural modification.[127] The rutile $TiO_2$ (110) surface reconstructs and restructures at high temperatures under both oxidizing and reducing conditions.[127] The $TiO_2$ (110) surface consists of alternating rows of 2-fold-coordinated bridging $O_b$ oxygen ions


dx.doi.org/10.1021/cr400624r | Chem. Rev. 2014, 114, 9890−9918

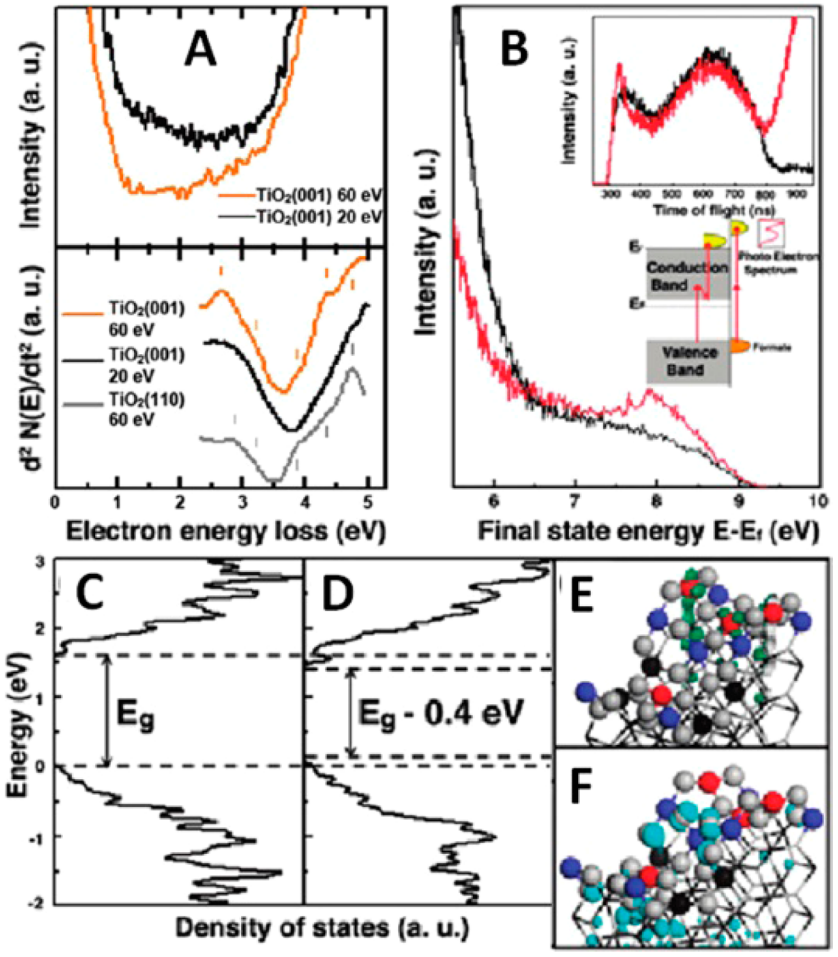


**Figure 3.** Electron energy-loss spectra (A), two-photon photoelectron spectra before (black) and after (red) exposure to formic acid (B), density-of-states of $TiO_2$ (110)−1 × 1 structure (C) and $TiO_2$ (001) latticework structure (D), and orbitals of the CBM (E) and VBM (F).[160] (Reprinted with permission from ref 160. Copyright 2009 American Chemical Society).

and 5-fold-coordinated $Ti_{5c}$ titanium ions in the [001] direction.[127] It relaxes mainly perpendicularly to the surface (Figure 2).[127] The $O_b$ atoms relax downward considerably, the $Ti_{5c}$ atoms move downward, and the lower $Ti_{6c}$ atoms relax upward.[127,148−151] This results in a smaller bond length (1.71 Å) between $Ti_{6c}$ and $O_b$ than that of the bulk Ti−O value (1.95 Å).[148−151] In practice, surface oxygen vacancies and interstitial titanium species were commonly observed during sample preparation,[127,152,153] and a band-gap state with Ti 3d character was found 1 eV below the Fermi level ($E_F$) as a result.[154−157] It was suggested that the neighboring empty $Ti_{5c}$ 3d orbitals accepted two excess $O_b$ electrons, producing two $Ti^{3+}$ sites.[154] The surface band-gap state of rutile $TiO_2$ (110) with the $V_O$ origin was confirmed by the observation that the intensity of the photoemission of the band-gap state was directly proportional to the $O_b$ density created with electron bombardment by Yim et al.[158] Moreover, Papageorgiou et al. showed that the negatively charged oxygen vacancies acted as trapping centers and largely influenced the reaction of molecular oxygen with surface hydroxyl at the vacancies.[159]

Ariga et al. reported that the (001) surface showed visible-light activity on photooxidation of formic acid.[160] The electron energy-loss spectrum showed a peak around 2.6 eV under an excitation energy of 60 eV, while no peak was observed under 20 eV (Figures 3A).[160] This suggested that the 2.6 eV excitation was likely near the surface.[160] In the two-photon photoelectron spectrum (inset in Figure 3B) the clean $TiO_2$ (001) surface showed a peak with a 340 ns flight time when excited with a 4.66 eV laser.[160] This corresponded to a final energy value of 8.2 eV (Figures 3B) and an initial energy of 1.1 eV below the $E_F$ on the clean surface.[160] The $TiO_2$ (001) surface had a smaller band gap than $TiO_2$ (110) (Figure 3C and 3D).[160] The $Ti^{4+}$ and oxygen orbitals on the surface contributed to the energy levels near the conduction band minimum (CBM) and valence band maximum (VBM), respectively (Figure 3E and 3F), causing band-gap narrowing.[160]

Tao et al. found that a reduced band gap of 2.1 eV was observed on rutile $TiO_2$ (011) surface by oxidation of bulk titanium interstitials.[161] The VBM of the pristine surface occurred at 3.0 eV, while the new (011) surface structure had extra states within the bulk band gap with a maximum at 2.1 eV below $E_F$ (Figure 4A and 4B).[161] The new (011) surface moved the VBM toward $E_F$ by ∼0.3 eV.[161] Upon high-temperature annealing, its electronic valence-band structure was regained (Figure 4A).[161] $Ti^{4+}$ was the charge state of the Ti atoms at the surface for the new (011) surface structure (Figure 4C).[161] A band gap reduced by 0.9 eV was achieved with this new rutile (011) surface (Figure 4D).[161]


dx.doi.org/10.1021/cr400624r | Chem. Rev. 2014, 114, 9890−9918

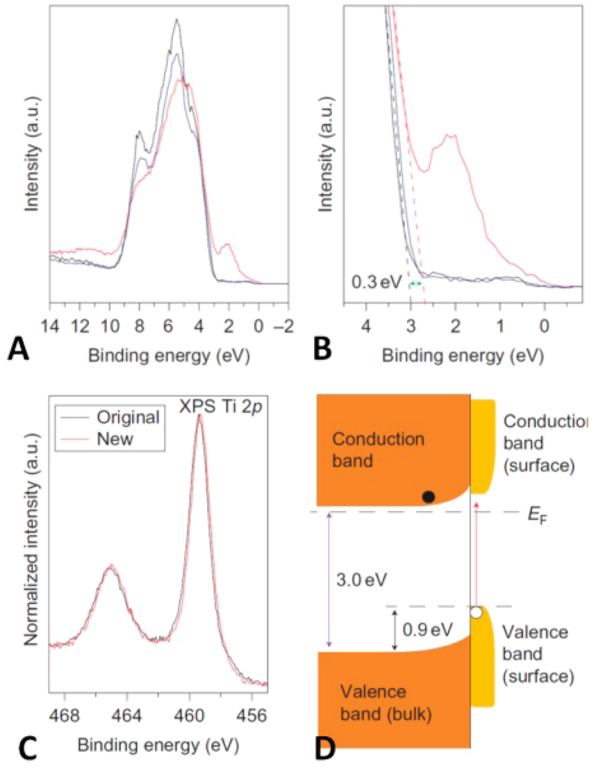


**Figure 4.** (A) Ultraviolet photoelectron spectra (UPS) of the original (2 × 1) surface (black curve), new surface $TiO_2$ (011) phase (red curve), and reformed (2 × 1) surface structure (blue line); (B) zoomed-in view of UPS; (C) Ti 2p core-level X-ray photoelectron spectra (XPS) before (black curve) and after (red curve) oxygen treatment; (D) band diagram of the (011) surface compared with the bulk.[161] (Reprinted with permission from ref 161. Copyright 2011 Macmillan Publishers Ltd.)

### 3.2. Lattice Strain Effects

While structural modification can tune the electronic properties of $TiO_2$ on the surface, it can also happen to the bulk phase with deviated lattice parameters, i.e., under lattice strain. Lattice strain effects can be observed at the interfaces between two phases of mismatched lattice and bonding structures. Shibata et al. found anatase film with strain had better photoinduced hydrophilic activity than that without strain;[162] Tavares et al. reported that polycrystalline $TiO_2$ thin films with strain showed largely enhanced photocatalytic activity,[163] and Kamei et al. attributed the enhanced electron−hole charge separation capability of anatase film to strain.[164] Anatase possesses a low density due to the strong repulsion between Ti ions across the shared edges of distorted $TiO_6$ octahedra.[165] This causes structural elongation and shrinkage along and normal to the *c* direction, respectively, in the $TiO_6$ octahedra.[165] Figure 5 displays the changes of the relative unit cell parameters under pressure and *d* spacing deduced from the X-ray diffraction (XRD) data for 6 nm anatase in contrast with standard Au.[166] A larger linear compressibility along the *c* axis than along the *a* axis was observed under the anisotropic compression of bulk anatase (at $P < 10$ GPa).[167,168] Upon compression it was relatively easy to shorten along the *c* axis in the $TiO_6$ octahedra as a result of the Ti−Ti repulsion.[167,168]

Lattice strain effects are also observed when the lattice parameters of the bulk materials are different from the normal values under standard conditions. For example, compressing or stretching the crystal with external forces would lead to shrinkage or elongation of lattice dimensions, which led to the electronic and optical property changes.[169] Softening of Ti−O bonds along the *c* or (001) direction provided an opportunity to tune the band gap of $TiO_2$ by applying stress along this direction, as demonstrated by Yin et al.[169] In deformation potential theory the band-gap change of a semiconductor under stress is given by

$$E_g(\sigma_a, \sigma_c) = E_g^0 + b_a\sigma_a + b_c\sigma_c \quad (1)$$

where $E_g^0$ is the band gap of unstrained bulk crystal and $b_a$ and $b_c$ are the band-gap pressure coefficient of epitaxial and uniaxial stress, respectively.[170,171] The hydrostatic band-gap pressure coefficient is $b_a + b_c$. Yin et al. found that when applied stress was along its soft direction the band-gap change of anatase was more obvious based on their density functional theory (DFT) calculations within the generalized gradient approximation (GGA) (Figure 6).[169] $b_c$ and $b_a$ were 35.3 and 39.8 meV/GPa, respectively. These results indicated that the compressive stress along the *c* axis was easier than in the *xy* plane to reduce the band gap as $|b_c| > |b_a|$.[169] Under a pressure of up to 10 GPa the band-gap change of rutile was smaller than 0.08 eV, as the soft axes in rutile are along both the (110) and the $(1\bar{1}0)$ directions, but all of the soft axes lie along the (001) direction in anatase.[169] A similar conclusion was obtained with a $b_a$ of 43.51 meV/GPa in the calculation by Thulin and Guerra.[172]

### 3.3. Nanoscale Effects

On the basis of the surface and lattice strain effects on the electronic band structures of $TiO_2$ it is thus reasonable to understand the observed electronic and optical property changes besides those caused by the small size of nanomaterials. The effects caused by the size are normally called size effects. Besides the size effects, the nanoscale effects also include the effects caused by the shape and lattice parameter changes of the nanocrystals from the bulk counterparts. As in nanomaterials, the percentage of surface atoms increases significantly with the decrease of the material size, and the lattice parameters are normally different from the bulk values.[123,124,173] Nanomaterials, especially semiconductors in nanoscale, are usually characterized by the quantum size effect.[123,124] When the size decreases, the band becomes discrete, the band gap of nanoparticles increases,[174−178] and the charge carriers behave quantum mechanically.[123,124,179] These changes are more easily observed when the size of these particles approaches the Bohr radius of the first excitation state or the de Broglie wavelength of their electrons and holes. The band-gap energy $E_g$ and the radius *R* of the nanoparticles have the following relationship

$$E_g \approx E_g^0 + \frac{h^2}{8\mu' R^2} - \frac{1.8e^2}{\varepsilon' R} \quad (2)$$

where *e*, *h*, $E_g^0$, $\varepsilon'$, and $\mu'$ are the electron charge, Planck constant, bulk band gap, apparent dielectric constant of the semiconductor, and apparent reduced mass of the electron and hole in the quantum region, respectively.[177,178] The $\mu'$ value of $TiO_2$ is around 1.63 $m_0$ (where $m_0$ is the electron rest mass),[176] and the $\varepsilon$ values are 31 and 173 for anatase and rutile, respectively.[180] A clear band-gap shift was observed as $2R < 2$ nm, and the difference in $E_g$ between the rutile and anatase decreased as the 2*R* value was close 1 nm, as shown in Figure 7.[181]

Quantization effects apparently depend on the nanomaterial's critical size. The estimated critical diameter is largely influenced


dx.doi.org/10.1021/cr400624r | Chem. Rev. 2014, 114, 9890−9918

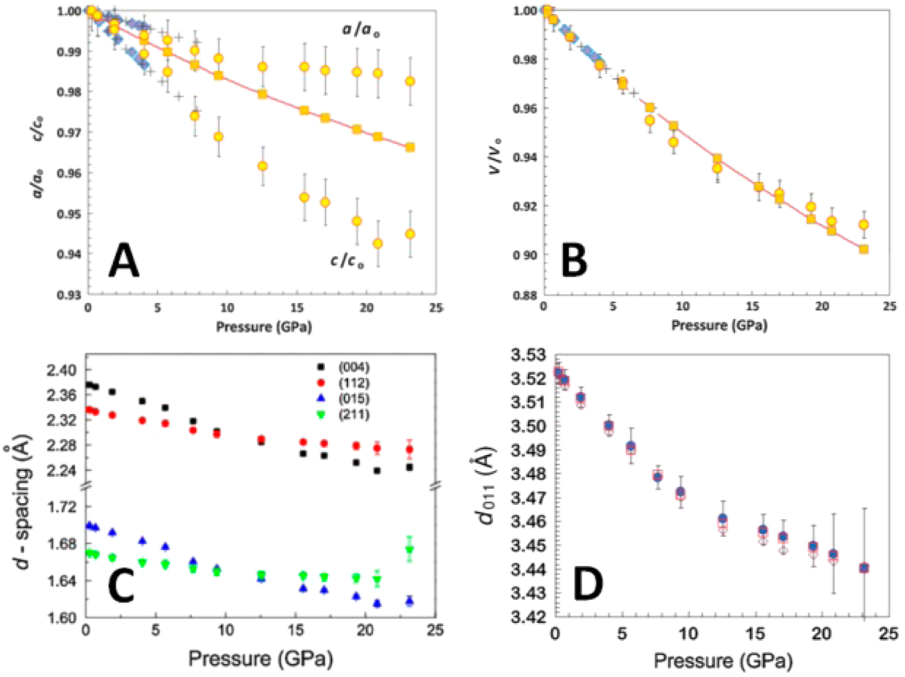


**Figure 5.** Change of the relative unit cell constants under pressure. (A) $a/a_o$ for Au (squares) and $a/a_0$ and $c/c_o$ for anatase; (B) $V/V_O$ vs pressure for Au and anatase. (◇) Single-crystal data from ref 167; (+) microparticle data from ref 168; (o) 6 nm anatase.[166] (C) Changes in the (004), (112), (105), and (211) *d* spacings. (D) Pressure vs *d* (0111) of anatase obtained via single-peak fit together with Au data collected near the center of the diamond-anvil cell (diamonds), single-peak fit (sample away from Au) (squares), and full-spectrum fit of anatase XRD collected away from the diamond-anvil cell center (filled circles with error bars).[166] (Reprinted with permission from ref 166. Copyright 2009 The American Physical Society.)

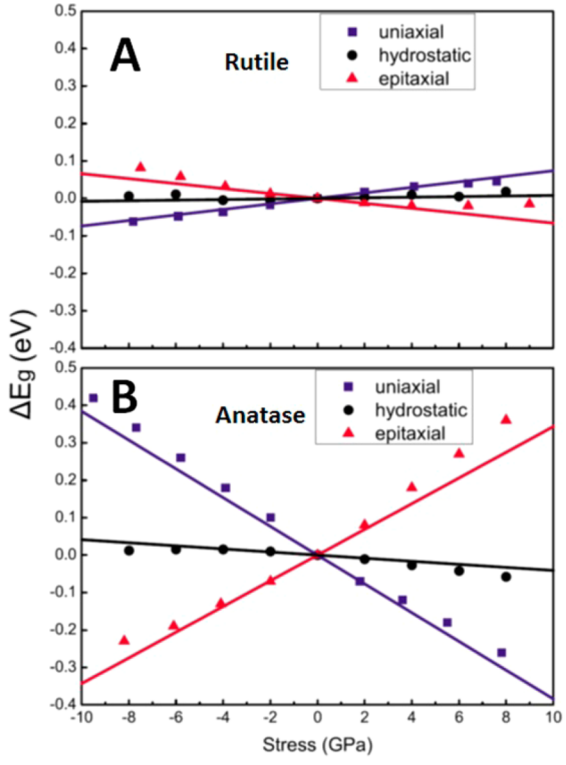


**Figure 6.** Band-gap change in rutile (A) and anatase (B) under stress: (dots) calculated results, (lines) fittings.[169] (Reprinted with permission from ref 169. Copyright 2010 American Institute of Physics.)

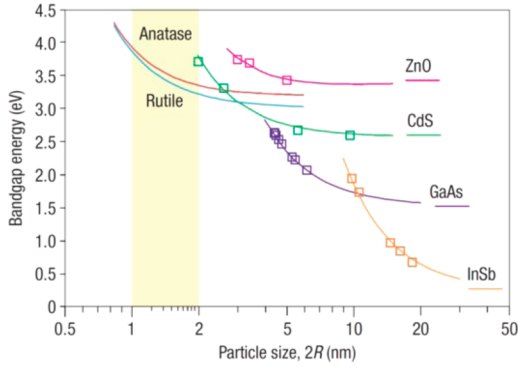


**Figure 7.** Calculated $TiO_2$ band-gap energy change with size: (□) experimental data.[181] (Reprinted with permission from ref 181. Copyright 2008 Nature Publishing Group.)

by the effective masses of the charge carriers, and this critical size for $TiO_2$ was around 2 nm, although with some small discrepancies.[174,176,182−186] This size was suggested to be below 2.1 nm, since no blue shift was seen in the optical absorption edges when $2.1 < 2R < 26.7$ nm.[184] The excitation radii range was estimated to be within 7.5−19 Å,[176] and a small apparent band-gap blue shift (<0.1−0.2 eV) was observed for size < 2 nm.[182,183] This observation was attributed to the relatively high effective mass of carriers.[176] Thus, the blue shifts for $TiO_2$ with sizes of 21, 133, and 267 Å were suggested to not be due to the quantum confinement effect.[184] No quantum-size effect was found in anatase $TiO_2$ nanoparticles of sizes $2R \geq 1.5$ nm.[186]

The electronic properties of small $TiO_2$ clusters have been studied both theoretically and experimentally.[187−192] Zhai and Wang investigated a series of $(TiO_2)_n$ clusters' electronic structures and the evolution of their band gap as a function of size.[189,190] They prepared the $(TiO_2)_n^-$ clusters by laser vaporizing Ti in He gas containing 0.5% $O_2$.[188] The lowest


dx.doi.org/10.1021/cr400624r | Chem. Rev. 2014, 114, 9890−9918

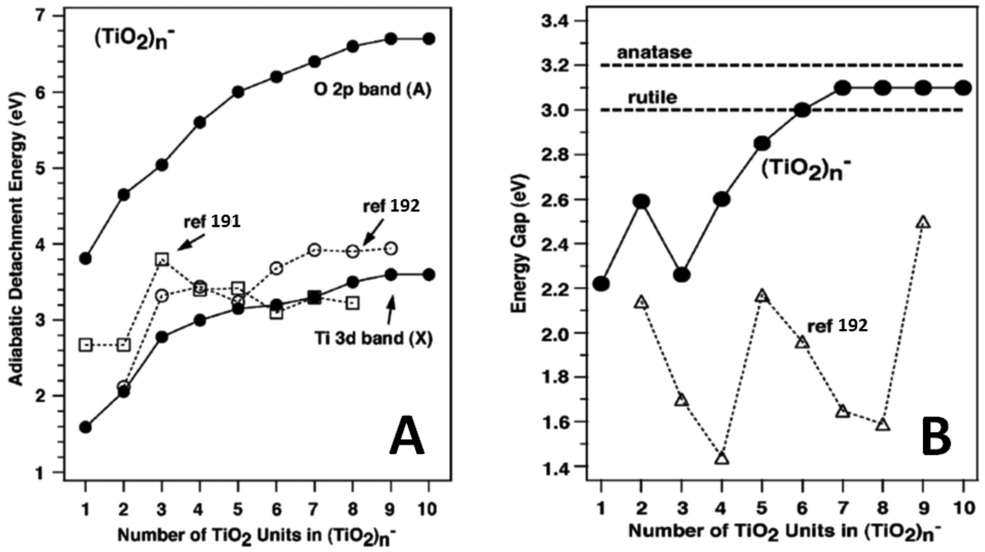


**Figure 8.** (A) Observed adiabatic detachment energies (solid dots) for the Ti 3d band and O 2p band of $(TiO_2)_n^-$ ($n$ = 1−10). Key: (□) LUMO energies from ref 191; (○) adiabatic electron affinities from ref 192. (B) Observed HOMO−LUMO energy gaps of $(TiO_2)_n^-$ ($n$ = 1−10). $TiO_2$ bulk limits (rutile, 3.0 eV; anatase, 3.2 eV) are shown as horizontal dashed lines. (Δ) Theoretical results from ref 192.[190] (Reprinted with permission from ref 190. Copyright 2007 American Chemical Society).

unoccupied molecular orbitals (LUMOs) and highest occupied molecular orbitals (HOMOs) of the $(TiO_2)_n$ clusters were mainly from O 2p orbitals and Ti 3d orbitals, respectively.[190] The LUMOs and HOMOs of $(TiO_2)_n$ clusters evolved into the bulk conduction and valence bands.[190] As the extra electron in the $(TiO_2)_n^-$ anion occupied the Ti 3d-based LUMO of neutral $(TiO_2)_n$, these anion clusters were like $Ti^{3+}$ centers on the $TiO_2$ surfaces with the dominating $Ti^{3+}$ sites.[190] Figure 8A shows the observed adiabatic detachment energies for the Ti 3d and O 2p bands of the $(TiO_2)_n^-$ ($n$ = 1−10), and Figure 8B shows the corresponding HOMO−LUMO energy gaps along with some theoretical calculation results.[191,192] Apparently, the adiabatic detachment energies for the Ti 3d and O 2p bands and HOMO−LUMO energy gaps of the $(TiO_2)_n^-$ increased as $n$ increased. The energy gap approached the bulk limit at $n$ = 6 and remained almost unchanged for $n$ = 6−10.[190]

Some theoretical studies have also been carried out on the electronic properties of $(TiO_2)_n$ clusters.[191−194] Qu and Kroes studied the stability and electronic structure of $(TiO_2)_n$ clusters ($n$ = 1−9).[192] Some compact structures were formed with the lowest lying singlet clusters, which were more stable than the corresponding triplet structures.[192] The holes within $(TiO_2)_n^+$ clusters and the extra electrons within $(TiO_2)_n^-$ clusters preferred the least coordinated O and Ti atoms, respectively.[192] Both the cluster formation energy per $TiO_2$ unit and its electron affinity increased with cluster size $n$, whereas the ionization potential decreased.[192] Using DFT and time-dependent DFT(TDDFT), Shevlin and Woodley found that for bare and anion-doped nanoscale $(TiO_2)_n$ ($n$ = 1, 2, 3, 4, 5, 6, 7, 10, and 13) clusters, with increasing nanoparticle size, the HOMO−LUMO transition energy approached toward bulk values for small values of $n$ (Figure 9).[193] Chiodo et al. simulated atomic clusters of $TiO_2$ by ab initio molecular dynamics (MD), DFT, TDDFT, and many-body techniques and suggested that clusters with anatase symmetry were energetically stable and could be considered as the starting seeds to grow much larger and more complex nanostructures.[194] They found that the electronic gap of these inorganic molecules was larger than the optical gap by almost 4 eV with

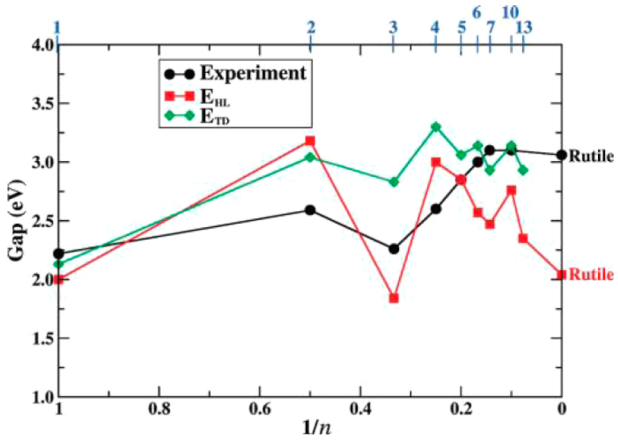


**Figure 9.** Plot of experimental gap ($E_{exp}$), DFT transition energy (HOMO−LUMO energy difference) ($E_{HL}$), and TDDFT singlet transition energy ($E_{TD}$), for inverse $n$. All units are in eV.[193] (Reprinted with permission from ref 193. Copyright 2010 American Chemical Society).

strong excitonic effects and that charge-transfer effects played an important role under photon absorption.[194]

Guisbiers et al. studied the change of melting temperature and band gap of $TiO_2$ nanomaterials caused by the size.[195] They found a structural phase transition from anatase to rutile starts around 40, 29, and 48 nm for nanoparticles, nanowires, and nanotubes, respectively.[195] For freestanding nanostructures the melting temperature $T_m$ at the nanoscale can be expressed as a function of bulk melting temperature $T_{m,\infty}$, size of the nanostructure, and some material properties

$$\frac{T_m}{T_{m,\infty}} = 1 + \frac{(\gamma_l - \gamma_s)}{\Delta H_{m,\infty}} \frac{A}{V} = 1 - \frac{\alpha_{shape}}{2L} \quad (3)$$

where $\Delta H_{m,\infty}$ is the melting enthalpy (J/m$^3$) and $\gamma_l$ and $\gamma_s$ are the surface energy in the liquid and solid phases (J/m$^2$), respectively.[195−197] $A$ (m$^2$) and $V$ (m$^3$) are the surface area and volume of the nanostructure. The shape parameter $\alpha_{shape}$ is


dx.doi.org/10.1021/cr400624r | Chem. Rev. 2014, 114, 9890−9918

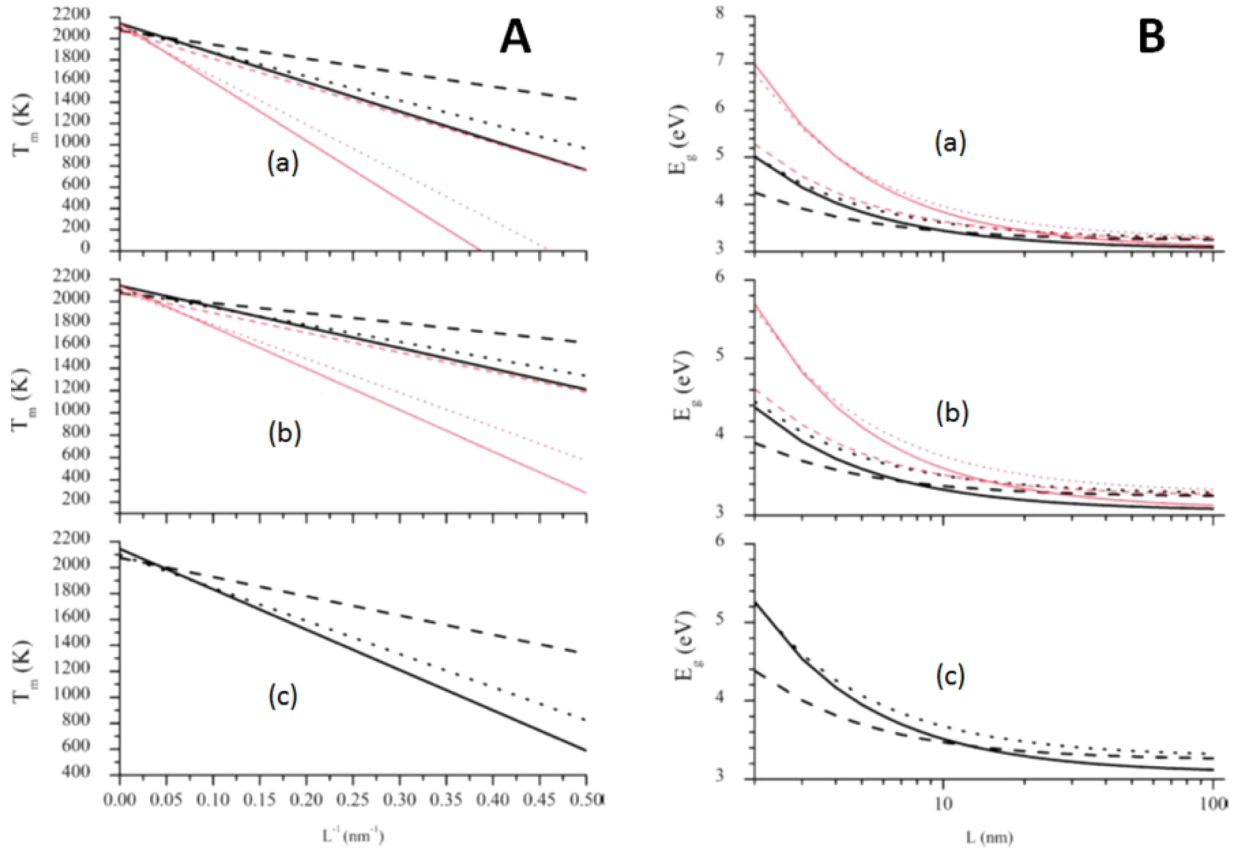


**Figure 10.** (A) Melting temperature and (B) band gap vs the (reciprocal) size for (a) spherical and cubic $TiO_2$ nanoparticles, (b) cylindrical and parallelepipedic $TiO_2$ nanowires with a length of 100 nm, and (c) cylindrical $TiO_2$ nanotubes with a length of 100 nm and a ratio of the outer-to-inner diameter equals 1.6. Solid, dashed, and dotted lines represent the rutile, anatase, and brookite phases, respectively. Thick black lines represent the nanostructures with a circular section, and thin red lines represent the nanostructures with a square section.[195] (Reprinted with permission from ref 195. Copyright 2008 American Institute of Physics.)

defined as $\alpha_{shape} = 2AL(\gamma_s - \gamma_l)/(V\Delta H_{m,\infty})$, where $L$ is the smallest dimension of the structure (i.e., for a sphere, $L = R$).[195−197] The authors pointed out that the size limit of thermodynamics is ~2 nm. The size effects on the melting temperature are shown in Figure 10A for different shapes of $TiO_2$ nanostructures.[195] For spherical nanoparticles, anatase was more stable when sizes were smaller than 40 nm.[195] The energy band gap of semiconductors was temperature dependent, which decreased as the temperature increased.[195,198] That was attributed to the increasing interatomic spacing as a result of the thermally enhanced atomic vibrations.[195] In response, the potential of the electrons decreased, reducing the band gap.[195] The effect of the size on the semiconductors' energy band gap can be described with the same $\alpha_{shape}$ parameter through the melting temperature's size dependence[199,200]

$$\frac{E_g - E_{g,\infty}}{E_{g,\infty}} = 1 - \frac{T_m}{T_{m,\infty}} = \frac{\alpha_{shape}}{2L} \quad (4)$$

The band gap increased and the melting temperature decreased when the size decreased, as illustrated in Figure 10B.[195] As they had the lowest $\alpha_{nanowire}$ value among the nanoparticles, nanowires, and nanotubes,[195] $TiO_2$ nanowires had a smaller band gap than $TiO_2$ nanoparticles and nanotubes.[195]

Due to the large specific surface area, the surface/interface effects count more in affecting the overall parameters of nanomaterials. An increase in a unit cell edge and a reduction in $c$ were observed experimentally for anatase nanoparticles < 10 nm[165,201−203] due to the weakened Ti−Ti repulsion and more regular $TiO_6$ octahedra in nanocrystalline anatase caused by the increased Ti vacancies.[165,201−203] Figure 11 shows the size-dependent variations of the anatase unit cell constants relative to bulk values.[166]

The anatase−rutile phase transition has been widely observed for $TiO_2$ and was believed to involve the interfaces in between and the coalescence of several "prior" anatase particles.[131,144,204−207] It was found that the thermal stability of nanocrystalline anatase $TiO_2$ and anatase−rutile phase trans-

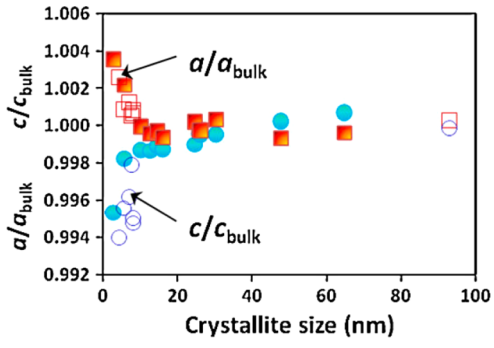


**Figure 11.** Size-dependent variations of the anatase unit cell constants relative to bulk values:[166,195] (solid symbols) ref 201; (open symbols) ref 203. (Reprinted with permission from ref 166. Copyright 2009 The American Physical Society.)


dx.doi.org/10.1021/cr400624r | Chem. Rev. 2014, 114, 9890−9918

formation were size dependent.[139,142,208] Phase transformation occurred at lower temperatures in smaller anatase nanoparticles than in larger ones.[191] Gribb and Banfield found that when the reacting crystalline anatase was very small the anatase-to-rutile transformation rate increased rapidly.[139] Anatase coarsening and rutile formation occurred at the same time, and the rate of transformation depended upon crystallite size.[139] Zhang et al. suggested the phase transformation of anatase $TiO_2$ nanoparticles was a size-dependent outer/inner mechanism.[208] They found that size was the critical parameter.[208] For particles with diameters less than 60 nm, rutile nucleated at anatase interfaces, while for larger particles, rutile nucleated in the interfaces and the bulk as well as on the free surface.[208] Satoh et al. found the anatase−rutile phase transition was both irreversible and size dependent.[209] They proposed the nucleus-sized crystal phase depended on the coordination sites, cis or trans, in the $TiO_6$ octahedra.[209] Lin et al. found that higher photocatalytic activity in the decomposition of 2-chlorophenol was seen on $TiO_2$ nanoparticles with smaller sizes.[210] They also suggested that the primary particle size was a good parameter to predict the photocatalytic rate, as it was closely related to the electro-optical properties of photocatalysts.[210]

Thus, even for pure $TiO_2$ nanomaterials with different sizes, shapes, and surface morphologies, their structural characteristics may differ enough to allow self-structural modifications to achieve tunable electronic, optical, and photocatalytic properties.

## 4. SELF-STRUCTURAL MODIFICATIONS IN MIXED PHASES

### 4.1. Improved Photocatalytic Performance

Degussa P25 has been widely used as a reference photocatalyst in photocatalytic studies.[20] Degussa P25 is a made of 70 wt % anatase and 30 wt % rutile and has a surface area of 55 $m^2\ g^{-1}$ with an average size of 30 nm.[20] Ohtani et al. isolated anatase and rutile from Degussa P25 by selectively dissolving them using hydrogen peroxide/ammonia and hydrofluoric acid, respectively.[118] They found that besides the anatase and rutile a small amount of amorphous phase also existed. Mixed anatase/rutile including P25 displayed enhanced photocatalytic performance over pure anatase or rutile nanocrystals.[211−216] When these mixed phases were constructed into hollow microspheres they showed further increased photovoltaic and photocatalytic performance.[105] Anatase/brookite mixture powders, prepared from thermal hydrolysis of titanium bis(dihydroxide) at lower urea concentrations, also showed better photocatalytic $H_2$ generation activity over $TiO_2$ Degussa P25, as shown in Figure 12.[120] Other mixed phases of $TiO_2$ have also been reported, such as biphase anatase/brookite $TiO_2$ mesoporous hollow spheres.[217] Zhao and Chen et al. synthesized these submicrometer hollow spheres (23% brookite phase + 77% anatase phase) via the Ostwald ripening process with a biocompatible oxalic acid, and these spheres displayed good performance in photocatalytic degradation of phenol and RhB.[217]

### 4.2. Synergistic Effects

Synergistic effects are often used to explain the enhanced photocatalytic performance of anatase/rutile nanocomposites over pure anatase or rutile nanocrystals.[211−216] It was suggested that rapid electron transfer from rutile to anatase occurred at the interface between these two phases.[211,212] An antenna function was suggested for the rutile phase to extend the photoactivity into visible wavelengths as well as catalytic "'hot spots'" at the rutile−anatase interface.[211] The work function difference across anatase and rutile interface was suggested to form a built-in electric field at the interface which facilitated the interfacial charge transfer.[214] The interface was key for the enhanced photocatalytic efficiency.[216] It was also pointed out that catalytically active surfaces were disordered, while ordered surfaces were inactive.[218−222]

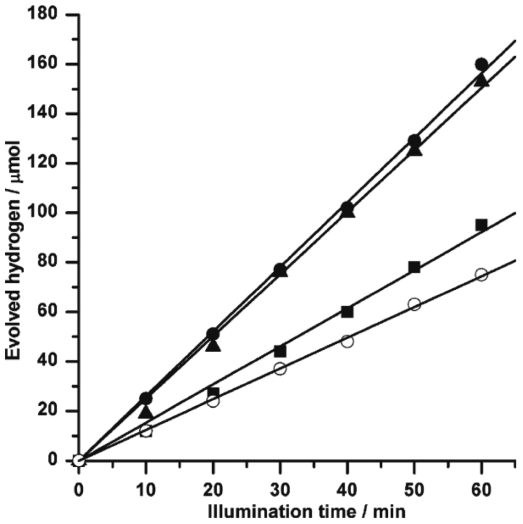


**Figure 12.** $H_2$ evolution over Pt-loaded (■) anatase nanoparticles, (●) anatase/brookite mixture (28% brookite and 72% anatase), (▲) brookite nanorods, and (○) Degussa P25; 0.5 g $L^{-1}$ catalyst, 75 mL of aqueous methanol solution (4.93 mol $L^{-1}$), 0.5 wt % Pt, and UG1 black filter.[120] (Reprinted with permission from ref 120. Copyright 2010 American Chemical Society.)

Charge transfer across the anatase/rutile phases apparently contributed to the synergistic effects, and the charge-transfer direction depended on the relative band edge positions of these two phases.[223] Keven et al. found that anatase (101)'s conduction band edge was 0.2 eV higher than rutile (001)'s from the fact that anatase's flat band potential was ∼0.2 eV more negative than rutile's from their electrochemical impedance analysis.[224] This band alignment favored the photoexcited electrons' transfer from anatase to rutile and the holes from rutile to anatase, which was supported by evidence from photocatalytic[225,226] and photoluminescence studies.[227] The conclusion was also based on the assumption that the interfacial structure between the anatase and the rutile phases was made of anatase (101) and rutile (001).[223] Xiong et al. found that the rutile's $E_F$ level laid 0.2 eV above anatase's based on their work function measurements with photoelectron spectroscopy.[228] On the other hand, Deak et al. suggested that the bulk rutile's conduction and valence-band edges laid about 0.3−0.4 and 0.5−0.6 eV above anatase's, respectively.[119] Scanlon et al. performed both theoretical calculations and experimental measurements and found that rutile's conduction and valence-band edges were 0.22 and 0.44 eV higher than anatase's.[223] The latter band alignment favored photoelectron transfer from rutile to anatase and holes from anatase to rutile.[119,223,228] Both alignments apparently (Figure 13) explained the synergistic effects between these two phases.[223] However, in these measurements model systems were commonly employed, providing clean surfaces.[223] In many photocatalytic systems, nanocrystalline anatase/rutile mixtures used had unavoidable surface defects. Practical band alignments


dx.doi.org/10.1021/cr400624r | Chem. Rev. 2014, 114, 9890−9918

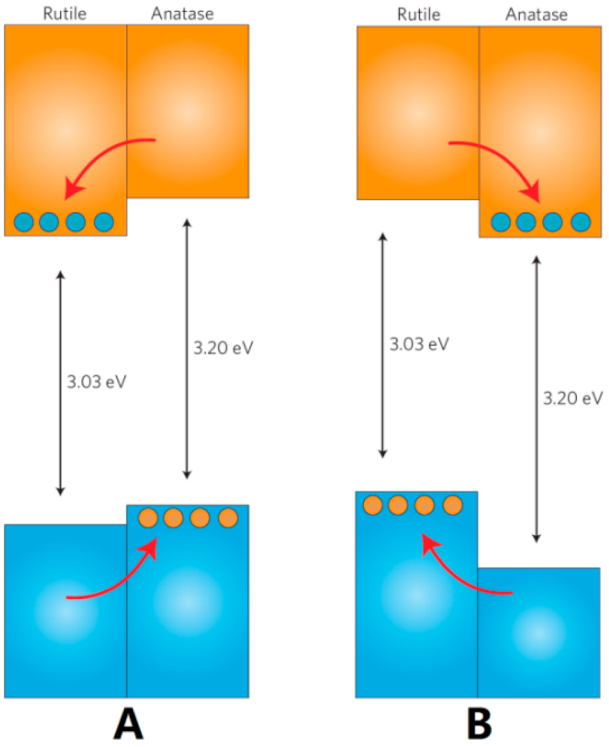


**Figure 13.** Two valence/conduction band alignment mechanisms for the anatase/rutile interface:[223] (A) Type I (rutile)[162−165,224−227] and (B) Type II (anatase).[119,223,228] Red arrows indicate the flow of electrons (holes) in the conduction band (valence band). Blue and orange dots represent electrons and holes, respectively.[223] (Reprinted with permission from ref 223. Copyright 2013 Macmillan Publishers Ltd.)

between anatase and rutile thus may seem even more complicated given that the atomic arrangement in the anatase/rutile interface is still very elusive and under investigation.

### 4.3. Interfacial Structural Properties

Apparently, understanding the interfacial structure is the key to illuminating the relative electronic band positions of anatase and rutile and the flow direction of the photoelectrons and holes. It was suggested that within mixed-phase $TiO_2$ there were atypically interwoven small rutile and anatase crystallites.[211] Penn and Banfield observed with transmission electron microscopy (TEM) in the anatase particles oriented attachment induced twin formation along the (112) plane, and the adjacent ones were likely the nuclei of rutile, whose (010) planes were parallel to the (112) planes of anatase: $(010)_R//(112)_A$ (A, anatase; R, rutile).[207] Gouma and Mills found that in the selected-area electron diffraction (SAED) pattern of the anatase/rutile interface anatase's $[\bar{1}10]$ zone axis was parallel to the formed rutile's $[0\bar{1}1]$ zone axis, whereas anatase's $(\bar{1}12)$ planes were parallel to the rutile's $(\bar{2}00)$ planes.[144] An orientation relationship of the type $(011)_R//[110]_A$ and $(100)_R//(112)_A$ was concluded by their investigation.[144] Deskins et al. did the MD simulations with near-coincidence-site lattice theory and reported that anatase/rutile interfaces were slightly disordered, and the disorder was limited to a small interfacial region.[145] Due to surface rearrangements, rutile formation occurred at the anatase side of the interface and several interfaces, such as $(100)_R/(100)_A$ and $(110)_R/(101)_A$, were suggested.[145] They argued that the $(110)_R-(101)_A$ interfaces were preferred as the rutile (110) and anatase (101) surfaces were most abundant, (Figure 14A), and there

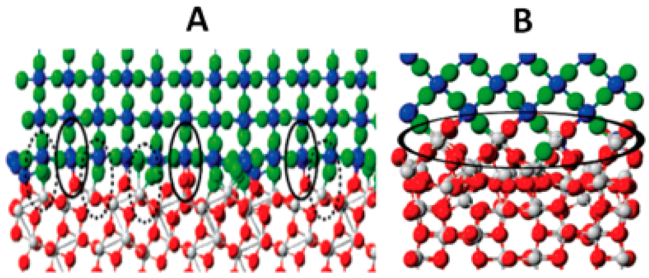


**Figure 14.** Interfaces between (A) (110) rutile and (101) anatase and (B) (100) ruitle and (100) anatase. Red and green spheres: O atoms from anatase and rutile, respectively. Gray and blue spheres: Ti atoms from anatase and rutile, respectively. Solid circled portions show the lifting of anatase surface O atoms to form six-coordinated rutile Ti, whereas dashed circled portions show $O_b$ bonding to anatase Ti atoms.[145] (Reprinted with permission from ref 145. Copyright 2007 American Chemical Society.)

appeared to be a very nice fit between the rutile (100) and the anatase (100) surfaces with a rearrangement of the top anatase layer to form a rutile-like layer (Figure 14B).[145]

Xia et al. suggested that the minority surfaces, rutile (101) and anatase (001), instead could form interfaces as they showed the closest bonding arrangements and parameters.[229] They built the interface by matching a $(1/\sqrt{2} \times 1/\sqrt{2})$ R45 rutile (101) cell (R45, rotated 45°) with 1 × 1 anatase (001) cell (Figure 15).[229] They found that the interfacial O 2p and Ti 3d orbital coupling was bigger than the bulk anatase, rutile, or anatase (001) and rutile (101) surfaces.[229] The computed band gap was 2.1 eV for the anatase (001)/rutile (101) interface, 2.3 eV for anatase (001) surface, 2.0 eV for rutile (101) surface, 3.0 eV for bulk rutile, and 3.2 eV for bulk anatase.[229] The interfacial band gap of the anatase (001)/rutile (101) was between those of the separate anatase (001) and rutile (101) surfaces.[229] They also found that the interface might absorb long-wavelength light, causing a directional heating effect across the anatase/rutile interface where the anatase phase gets much hotter than the rutile phase.[229]

Li et al. studied the interfacial structural and electronic properties of anatase (A), rutile (R), and brookite (B) composites.[230] They found that the HOMO−LUMO gaps of various surface slabs of the three phases were much smaller than the bulk values of these phases (see Table 2).[230] When the difference of the HOMO−LUMO gaps of the individual surface slabs was large [e.g., in the anatase−brookite (A−B, B−A) and the anatase−rutile (A−R, R−A) composites], the HOMO−LUMO gaps of the composites were between those of the individual surface slabs.[230] When the HOMO−LUMO gaps of the individual surface slabs were similar [R(011) and B(001)] the HOMO−LUMO gaps of the composites became either smaller or larger than those of the individual surface slabs, depending on the relative thickness of the each surface slab (see Table 2).[230] The locations of the HOMO and LUMO states in the composites depended on the compositions of the composites.[230] For the anatase A(110)−brookite B(010) composite both the HOMO and LUMO states were located in the anatase part of the composite; for the rutile R(011)−bookite B(001) composite the HOMO states stayed in the B(001) slab and the LUMO in the R(011); for the anatase


dx.doi.org/10.1021/cr400624r | Chem. Rev. 2014, 114, 9890−9918

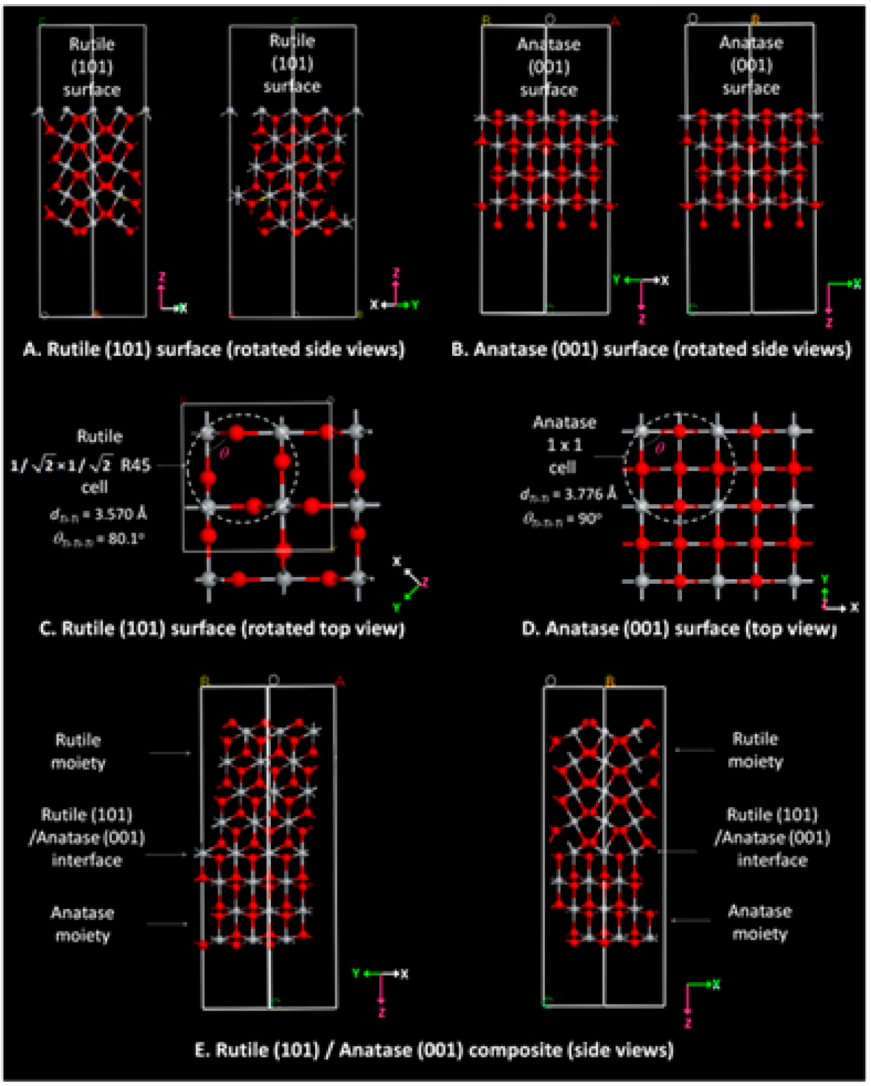


**Figure 15.** Crystal models of the $TiO_2$ rutile (101) surface (A), anatase (001) surface (B), $(1/\sqrt{2} \times 1/\sqrt{2})$ R45 (rotated 45°) cell in the rutile (101) surface (C), 1 × 1 cell in anatase (001) surface (D), and rutile (101)/anatase (001) interface (E) in the composite. Dashed lines in C and D highlight the junction cells in the composite.[229] (Reprinted with permission from ref 229. Copyright 2013 American Chemical Society.)

A(010)−rutile (011) composite, the locations of the HOMO and LUMO states depended on the thickness of each surface slab.[230]

In addition, Majumder et al. reported that crystalline $TiO_2$ nanodots formed on single-crystal rutile $TiO_2$ (110) surfaces via the ion-beam sputtering method displayed enhancement in visible-light absorbance and a smaller band gap.[231] These findings were consistent with the previous suggestion of the antenna effect of the rutile phase in extending the photoactivity into visible wavelengths and catalytic "'hot spots'" at the rutile−anatase interface by Hurum et al.,[211] the visible-light photochemical activity at the (001) surface by Ariga et al.,[160] and the observed reduced band gap of 2.1 eV of rutile $TiO_2$ (011) by Tao et al.[161] These results are not surprising but may provide us alternative routes in improving certain properties of $TiO_2$ nanomaterials, as defects, structural reconstruction, distortion, and disorders are generally expected on the surfaces of and in the anatase/rutile interfaces.

## 5. SELF-STRUCTURAL MODIFICATIONS IN AMORPHOUS/DISORDERED PHASES

Rahman et al. reported that the amorphous $TiO_2$ structure was not a good photocatalyst because of its large band gap and the structural disorder.[232] Kaur and Singh reported that amorphous $TiO_2$ nanomaterials had characteristic structural and electronic properties.[233] They studied three bulk $TiO_2$ models with supercell dimensions of 2 × 2 × 3 (72 atoms), 2 × 2 × 4 (96 atoms), and 3 × 3 × 4 (216 atoms) based on the MD simulations with Perdew−Burke−Erzerhof (PBE) DFT functionals.[233] They found that most Ti−O bond lengths were between 1.86 and 2.1 Å, whereas crystalline rutile Ti−O bond lengths were at 2.017 and 2.05 Å.[233] They found a relatively larger band gap and more band tail states for amorphous $TiO_2$ compared to rutile and anatase.[233] They suggested that band tail states were localized due to disorders of the bond angle and the positions of O and Ti atoms. Higher disorder resulted in more tailing bands in the band gap.[233]


dx.doi.org/10.1021/cr400624r | Chem. Rev. 2014, 114, 9890−9918

Table 2. Calculated HOMO−LUMO Energy Gaps[230]

| surface slab | energy gap/eV | composite | energy gap/eV | composite | energy gap/eV |
|---|---|---|---|---|---|
| A(110)[a] | 1.84 | | | | |
| | | A−2B[b] | 2.02 | B−2A | 2.41 |
| | | A−3B | 2.00 | B−3A | 2.31 |
| | | A−3B-2[c] | 1.90 | | |
| | | A−4B | 1.99 | B−4A | 2.10 |
| | | A−4B-2 | 1.90 | | |
| B(010) | 2.46 | | | | |
| R(011) | 1.86 | | | | |
| | | R−2B | 1.77 | B−2R | 1.93 |
| | | R−3B | 1.64 | B−3R | 1.97 |
| | | R−4B | 1.77 | B−4R | 1.71 |
| B(001) | 1.83 | | | | |
| R(011) | 1.86 | | | | |
| | | R−2A | 1.74 | A−2R | 1.66 |
| | | R−3A | 1.34 | A−3R | 1.87 |
| | | R−4A | 1.75 | A−-4R | 1.75 |
| A(010) | 1.69 | | | | |

[a]A, B, and R represents anatase, bookite, and rutile phase, respectively. [b]A−2B refers to the 5-layer anatase/2-layer brookite composite. [c]A−3B-2 refers to a second possible structure of the 5-layer anatase/3-layer brookite composite.[230]

## 6. SELF-STRUCTURAL MODIFICATIONS IN HYDROGENATED PHASES

### 6.1. Research Progress in Applications

**6.1.1. Photocatalysis.** Thermal hydrogen ($H_2$) treatment has been used to enhance $TiO_2$'s photochemical properties.[234−242] Heller et al. found the photoactivity of $TiO_2$ was enhanced by treating it in $H_2$ at 550 °C due to the increased $E_F$ and the energy barrier which pushed electrons away from the surface.[237] Harris and Schumacher found that this treatment reduced bulk recombination centers and increased the lifetime of the holes.[234] They found the presence and effects of oxygen vacancies, $Ti^{3+}$ species, and hydroxyl groups but were not sure if the improved photoactivity was a result from all the species present or only some of them.[234] Khader et al. studied the hydrogen reduction mechanism within 300−500 °C by means of electrical conductivity.[238] Haerudin et al. studied the surface stoichiometry of $TiO_2$ with Fourier transform infrared (FTIR) spectroscopy after hydrogen treatment.[241] Liu et al. reported that $H_2$-treated $TiO_2$ had enhanced performance in sulfosalicylic acid's photodecomposition, and a suitable treatment temperature was around 500−600 °C.[242]

Chen et al. found that the optical absorption (Figure 16A and 16B) was dramatically changed and the photocatalytic activity was largely enhanced by the hydrogenation process besides the surface structural properties.[102] The starting $TiO_2$ nanocrystals were well crystallized, based on the clearly seen lattice fringes in the high-resolution TEM (HRTEM) image (Figure 16C).[102] The hydrogenated black $TiO_2$ nanoparticles' surfaces became disordered (Figure 16D), and this disordered layer's thickness was about 1 nm.[80,102,104,243−245] Hydrogenated $TiO_2$ nanocrystals displayed largely improved photocatalytic activity in decomposing methylene blue or phenol or in generating hydrogen from water/methanol solution.[102] They also reported the black $TiO_2$ nanocrystals' color did not change for more than 1 year after they were synthesized.[102] The hydrogenated black $TiO_2$ nanocrystals had a similar $Ti^{4+}$ bonding environment after hydrogenation, did not resemble the $TiO_2$ doped with carbon or other impurities, and had an apparent Ti−OH signal through XPS measurements.[102,243] Through theoretical calculation on the electronic structures they observed midgap states in disordered $TiO_2$ nanocrystals.[80,102] The higher energy part (~3.0 eV) was only from Ti 3d orbitals; the lower part (~1.8 eV) was mixed from both O 2p and Ti 3d orbitals.[102] The coupling of the hydrogen 1s orbital to the Ti atom did not contribute to either state.[102] Hydrogen passivated the dangling bonds and stabilized the disordered lattice.[102] Hydrogenation caused lattice disorder in black $TiO_2$ and helped Ti−O bond breakup and Ti−H and O−H bond formation.[80] Disordered lattice was suggested for causing the midgap states.[102] The valence-band edge's blue shift and the long-wavelength optical absorption were attributed to the lower energy midgap states lying below the $E_F$.[102] The enhanced photocatalytic activity was attributed to prevention of fast recombination photoexcited electrons and holes in the midgap states.[80,102]

Following this report, numerous studies have been carried out, both experimentally and theoretically, to investigate the fundamental properties and photocatalytic applications of hydrogenated black $TiO_2$ nanocrystals.[246−261] Wang and Li et al. reported that hydrogenated $TiO_2$ nanowires grown in fluorine-doped tin oxide glass substrate displayed enhanced optical absorption and photoelectrochemical water-splitting performance.[246] They attributed this enhancement to the increased oxygen vacancies that served as electron donors.[246] Meanwhile, Sn-metal deposition was apparently observed for the hydrogen-treated samples above 450 °C, but its role was not explicitly discussed or explained in the study.[246] Zheng et al. found that surface-hydrogenated anatase nanowire micro-

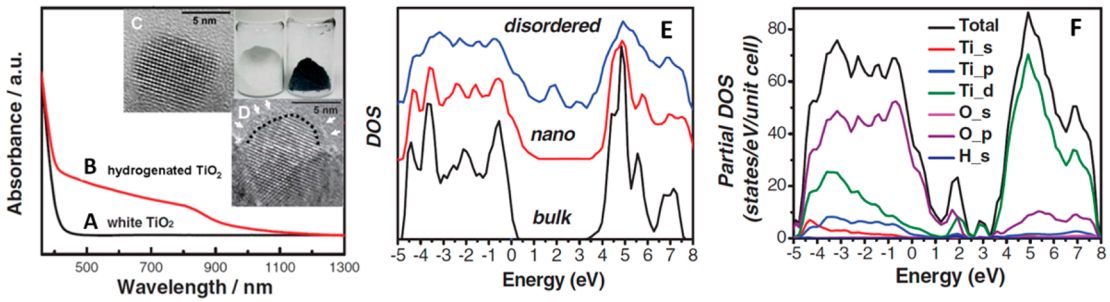


**Figure 16.** UV−vis spectra of pure white and hydrogenated black $TiO_2$. (Insets) Photo and HRTEM images of pure white $TiO_2$ (C) and hydrogenated black $TiO_2$ nanocrystals (D).[102] (Reprinted with permission from ref 102. Copyright 2011 The American Association for the Advancement of Science.)


dx.doi.org/10.1021/cr400624r | Chem. Rev. 2014, 114, 9890−9918

spheres prepared from protonated titanate nanotube under a hydrogen atmosphere exhibit enhanced absorption and photocatalytic activity in photodecomposition of 2,4-dichlorophenol in the visible-light region.[247] Wang and Xu et al. reported that hydrogenated $TiO_2$ nanosheets with exposed {001} facets showed a high and broad light absorption band toward the infrared range and enhanced its photocatalytic activity in decomposing methylene blue.[248] Wang and Jiang et al. produced black $TiO_2$ under hydrogen plasma featuring a crystalline core/amorphous shell structure and a strong absorption in the visible- and infrared-light region.[249−251] The large absorption was attributed to the localized surface plasmon resonance from the high carrier concentration in the amorphorized shell.[249−251] The black $TiO_2$ yielded large improvement in photocatalytic decomposition of methyl orange.[249−251] Leshuk et al. found that hydrogenated $TiO_2$ nanoparticles' optical properties strongly depended on the experimental synthesis parameters in hydrogenation processing, and worse photocatalytic activities were reported compared with pure $TiO_2$ nanocrystals.[250,251] Danon et al. reported that the color and stability of hydrogenated $TiO_2$ nanotubes were largely related to the type of reactors (glass, stainless steel, and quartz) in the hydrogenation process.[252] Yu et al. demonstrated that by tuning the hydrogenation conditions the photocatalytic activity of hydrogenated $TiO_2$ nanocrystals can be flexibly controlled, possibly due to the control of the bulk to surface defect distribution.[253] Lu et al. recently obtained hydrogenated $TiO_2$ nanocrystals by treating the commercial Degussa P25 under 35 bar hydrogen and room temperature up to 20 days, displaying black color and good photocatalytic activity in hydrogen generation.[254] Wei et al. found that hydrogenated {001}-facets-dominated anatase $TiO_2$ nanosheets had improved light absorption and enhanced photocatalytic activity, possibly from formation of Ti−H bonds, $Ti^{3+}$ ions, and oxygen vacancies produced by hydrogenation.[255] Zheng et al. suggested that the improved photoactivity of hydrogenated $TiO_2$ might come from the synergy of surface modification and morphology improvement.[247]

Li et al. reported an electrochemically hydrogen-modified anatase $TiO_2$ by cathodically biasing $TiO_2$ in an ethylene glycol electrolyte.[256,257] The resulting black $TiO_2$ had a significantly narrower band gap and higher electrical conductivity, with a largely improved photoconversion efficiency (increased from 48% to 72% in the visible region and from nearly 0% to 7% in the UV region).[256] Independently, Xu et al. reported that hydrogenated $TiO_2$ nanotubes obtained with an electrochemical reduction method showed improved performance in photoelectrochemical water splitting, possibly due to the surface oxygen vacancies.[258]

Buha reported that codoping with hydrogen in C-doped $TiO_2$ increased the fraction of the disordered phase and further narrowed the band by introducing the $Ti^{3+}$ states under the conduction-band edge, which potentially enabled sub-band-gap electronic transitions from the valence band and/or also enable charge trapping.[259] Hoang applied both hydrogenation and nitridation on $TiO_2$ nanowires and found that the visible-light performance in photo-oxidation of water was enhanced due to the N-dopant and $Ti^{3+}$ interaction.[260] Pan et al. found the effects of H and N doping on the photocatalytic and electronic properties of $TiO_2$ were phase dependent based on a first-principles study.[261] They believed that the improvement of the photocatalytic performance by (H, N)-*co*-doping was attributed to the enhanced visible-light absorption, reduced charge recombination centers, and increased charge mobility.[261]

**6.1.2. Lithium-Ion Battery.** $TiO_2$ has been suggested as a safer lithium-ion battery anode material over graphite.[262,263] Insertion/extraction of lithium proceeds within 1.5−1.8 V vs the $Li^+/Li$ redox couple in $TiO_2$, while it is close to zero for graphite.[262,263] The lithium and $TiO_2$ reaction is suggested as

$$TiO_2 + xLi^+ + xe^- \leftrightarrow Li_xTiO_2 \quad (5)$$

where $x$ is the molar fraction of Li in the $TiO_2$. Theoretically, a capacity value of 335 mAh $g^{-1}$ or 1.0 Li per $TiO_2$ can be realized.[262,263] Planar chains are formed in anatase $TiO_2$ by two $TiO_6$ octahedrons sharing two adjacent edges with two other neighbors.[264] Lithium ions travel through the octahedral interstitial sites.[265,266] As Li-ion insertion continues, the unit cell's symmetry decreases.[265,266] Due to the symmetry loss in the $y$ direction, the structure changes into orthorhombic $Pmn2_1$ from $I4_1/amd$ when $x = 0.5$ ($Li_{0.5}TiO_2$).[267] This induces a decrease in the $c$ axis and an increase in the $b$ axis and results in a ∼4% unit cell volume increase and a rapid fade in capacity for lithium storage.[268] Therefore, a maximum value of 0.5 for $x$ is frequently reported for bulk anatase $TiO_2$ for lithium storage.[50,269] Nanometer-scale spontaneous phase separation into $Li_{0.01}TiO_2$ and $Li_{0.6}TiO_2$ domains occurs in the anatase structure when Li is inserted.[270,271] The flat voltage curve in bulk anatase indicates a typical biphase Li insertion/extraction process.[270,271] Decreasing the size of the particles into the nanometer regime changes electrochemical reactions and lithium's reactivity.[272−274] The nanoscale Li insertion acts more like a solid solution.[272] Enhanced capacity larger than 0.5 Li per unit is expected upon size reduction and special morphologies of the electrode materials from surface-confined charge storage and distinct Li-reaction mechanisms.[272−274]

Shin et al. reported that hydrogenated $TiO_2$ nanocrystals displayed excellent rate performance for lithium storage.[275] The well-balanced $Li^+/e^-$ diffusion in the hydrogenated $TiO_2$ nanocrystals was the key factor for their high performance.[275] The hydrogen reduction reaction generated $V_O$ and increased the electronic conductivity.[275] Meanwhile, over-reduction was proven detrimental due to decreased free $Li^+$ concentration and extra electrons.[275] Lu and Zhou et al. reported that substantially improved high-rate performance was obtained by annealing anodized $TiO_2$ nanotubes in a reducing atmosphere (5% $H_2$ and 95% Ar) by hydrogenation process.[276] They suggested this rate improvement was due to the increase of electronic conductivity induced by a large number of oxygen vacancies produced from the hydrogenation treatment.[276] Under similar $H_2$ treatment, rutile nanowire arrays and anatase nanoparticles displayed enhanced rate capability as well.[276] Through electrochemical impedance measurement they found that hydrogenation apparently improved the electronic conductivity and $Li^+$-ion diffusion to facilitate the electrochemical reactions and improve the rate performance.[276] Improved lithium battery performance in the hydrogenated $TiO_2$ nanocrystals was reported by Xia et al. as well.[52] Li et al. found that hydrogenated mesoporous $TiO_2$ microspheres showed twice the rate capability compared to that of mesoporous $TiO_2$ microspheres due to the combination of the short lithium-ion diffusion path and the high electronic conductivity.[277] Their electrochemical impedance study also revealed that both the electronic conductivity and the lithium-ion diffusion kinetics were improved in the hydrogenation of $TiO_2$ microspheres (Figure 17).[277] Shen et al. found that hydrogenated $Li_4Ti_5O_{12}$


dx.doi.org/10.1021/cr400624r | *Chem. Rev.* 2014, 114, 9890−9918

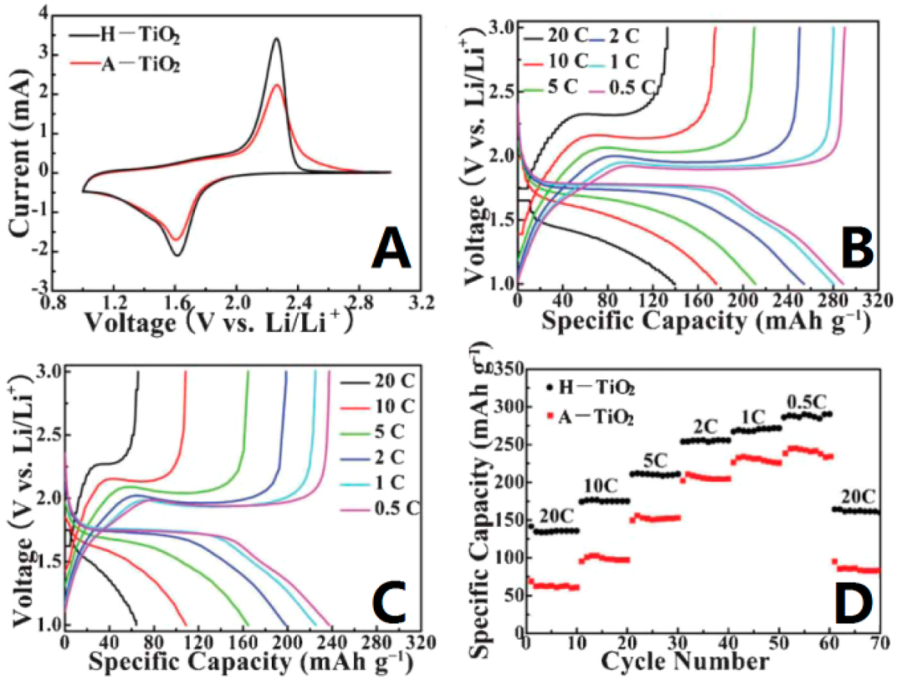


**Figure 17.** (A) Cyclic voltammetry profiles of the hydrogenated (H-$TiO_2$) and pure (A-$TiO_2$) anatase microspheres at a scan rate of 0.5 mV $s^{-1}$. Galvanostatic discharge−charge profiles of the (B) H-$TiO_2$ and (C) A-$TiO_2$ microspheres at various rates. (D) Comparison of the rate performance of the H-$TiO_2$ and A-$TiO_2$ microspheres.[277] (Reprinted with permission from ref 277. Copyright 2013 The Royal Society of Chemistry.)

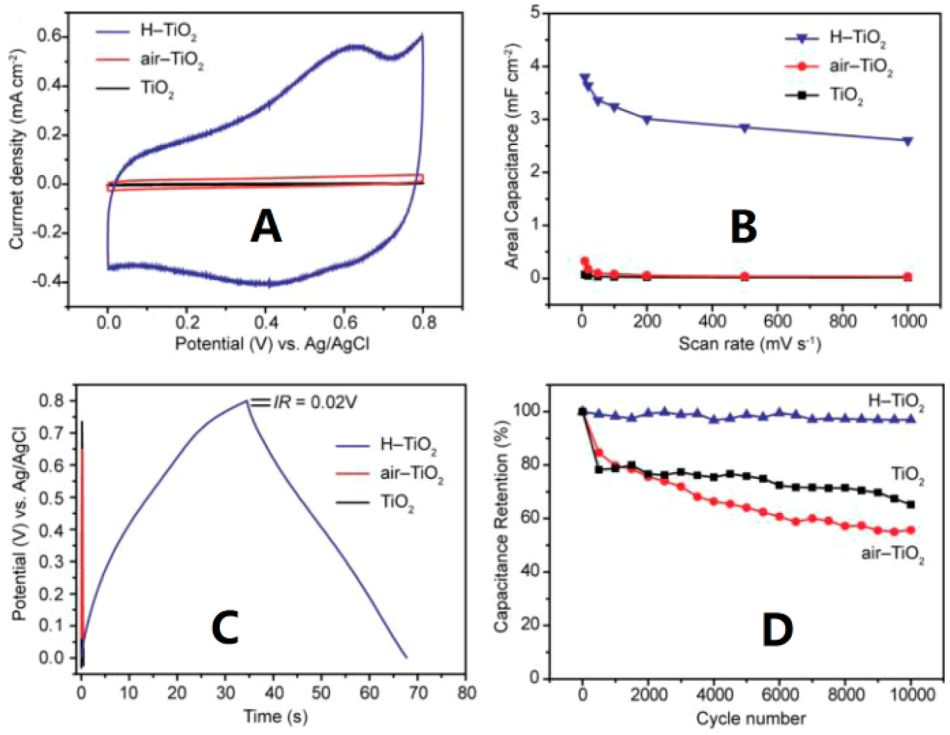


**Figure 18.** (A) Cyclic voltammetry curves at a scan rate of 100 mV $s^{-1}$, (B) areal capacitance as a function of scan rate, (C) galvanostatic charge/discharge curves collected at a current density of 100 $\mu$A $cm^{-2}$, and (D) cycle performance at a scan rate of 100 mV $s^{-1}$ of the untreated $TiO_2$, air-$TiO_2$, and H-$TiO_2$ nanotubes.[281] (Reprinted with permission from ref 281. Copyright 2012 American Chemical Society.)

nanowires enhanced lithium storage capacity by introducing $Ti^{3+}$ through hydrogenation due to higher electrical conductivity, which resulted in high capacity (173 mAh $g^{-1}$ at C/5), excellent rate performance (121 mAh $g^{-1}$ at 30 C), and good stability.[278] Myung et al. also found that nanostructured black $TiO_2$ had superior performance with a capacity of 127 mAh $g^{-1}$ at 100 C (20 A $g^{-1}$) and approximately 86% retention after 100 cycles at 25 °C.[279] Yang et al. reported on the fast lithium storage performance of hydrogenated anatase $TiO_2$ nanoparticles prepared by a $H_2$ plasma treatment.[280] Their cyclic voltammetry analysis revealed that the improved rate capability resulted from the enhanced contribution of


dx.doi.org/10.1021/cr400624r | Chem. Rev. 2014, 114, 9890−9918

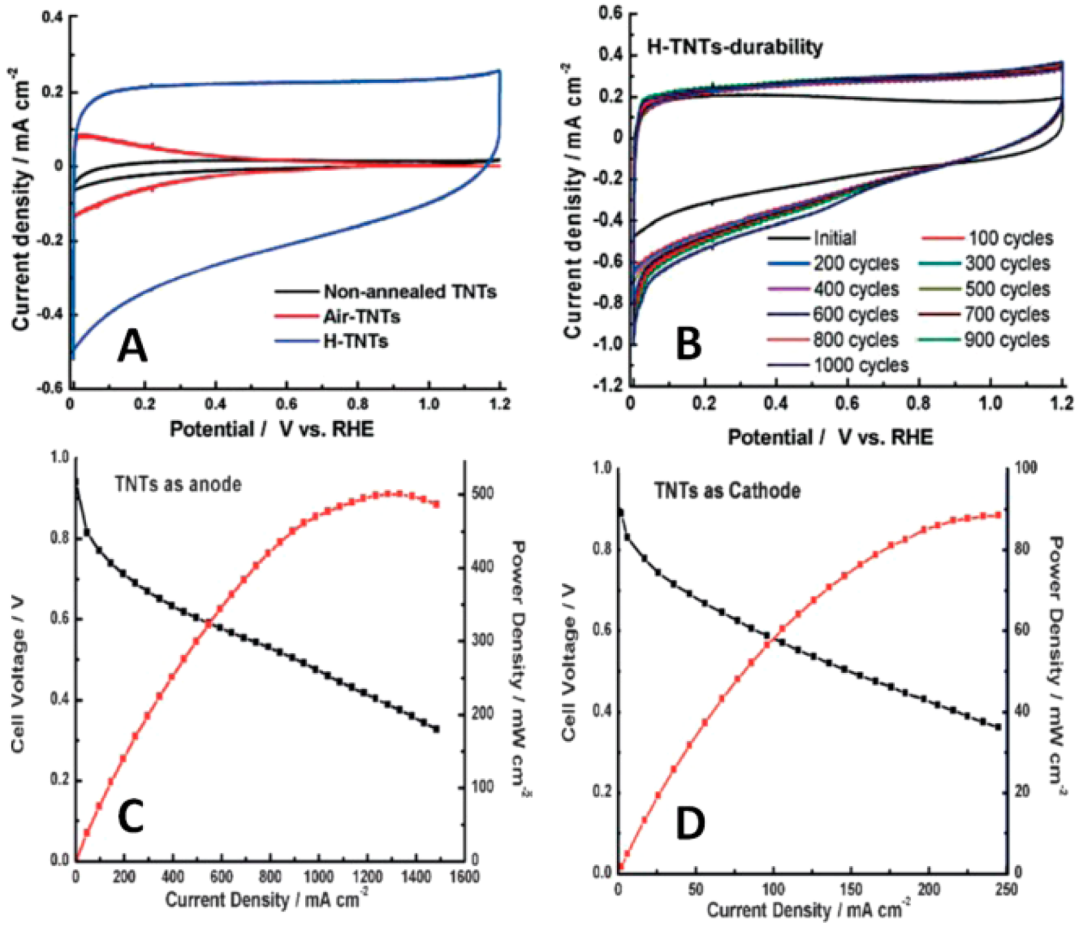


**Figure 19.** (A) CVs of the nonannealed TNTs, air-TNTs, and H-TNTs. (B) CVs of the H-TNTs electrode from initial cycle to 1000 cycles. Polarization curves using Pt−Pd−H-TNT−1−450−H as (C) the anode and (D) the cathode.[282] (Reprinted with permission from ref 282. Copyright 2013 Wiley-VCH Verlag GmbH & Co. KGaA, Weinheim.)

pseudocapacitive lithium storage on the particle surface, possibly due to the combined effect of the disordered surface layers and $Ti^{3+}$ species of H-$TiO_2$.[280]

**6.1.3. Supercapacitor.** Lu and Li et al. reported that hydrogenated $TiO_2$ nanotube arrays displayed improved performance as supercapacitors.[281] They prepared the hydrogenated $TiO_2$ nanotubes (denoted as H-$TiO_2$) by heating anodized $TiO_2$ nanotubes under hydrogen environment between 300 and 600 °C and found that when scanned at a rate of 100 mV $s^{-1}$ the sample obtain at 400 °C had a capacitance of 3.24 mF $cm^{-2}$, 40 times better than the air-annealed sample (Figure 18).[281] When the scan rate increased from 10 to 1000 mV $s^{-1}$, hydrogenated $TiO_2$ nanotubes showed excellent rate performance with 68% capacitance retention.[281] Hydrogenated $TiO_2$ nanotubes also had good long-term cyclic stability with 96.9% capacitance retention after 10 000 cycles.[281] The improved performance of hydrogenated $TiO_2$ nanotubes was due to increased densities of carrier and hydroxyl groups on $TiO_2$ surface from the hydrogenation.[281]

Li et al. also found that electrochemically hydrogen-modified anatase $TiO_2$ nanotubes by cathodically biasing $TiO_2$ in an ethylene glycol electrolyte displayed much higher performance as a supercapacitor electrode, possibly due to their high conductivities.[256]

**6.1.4. Fuel Cell.** Zhang et al. reported that hydrogen-treated $TiO_2$ nanotube (H-TNT) significantly improved fuel cells' performance and durability.[282] The H-TNTs' electrical conductivity (1.7 mS $cm^{-1}$) increased 10 times over air-treated TNTs (0.16 mS $cm^{-1}$).[282] The increased numbers of oxygen vacancies and hydroxyl groups on the H-TNTs helped to form uniform nucleation sites in anchoring a greater number of Pt nanoparticles.[282] The decrease in the electrochemical surface area of the H-TNT electrode was minimal after 1000 cycles, compared to a 68% decrease for the commercial 20% Pt/C electrode after 800 cycles (Figure 19).[282] In fuel-cell testing, the H-TNT displayed a maximum power density of 500 mW $cm^{-2}$ when used as anode and gave a specific power density of 2.68 kW g $Pt^{-1}$ when loaded with Pt as the cathode.[282]

**6.1.5. Field Emission.** Hydrogenated $TiO_2$ nanotube arrays dramatically improved their field emission properties (Figure 20).[283] The turn-on field of hydrogenated $TiO_2$ nanotubes decreased to 1.75 from 18.23 V $\mu m^{-1}$ and depended on the hydrogenation temperature.[283] Hydrogenated $TiO_2$ nanotube obtained at 550 °C showed a low turn-on field, a high current density (4.0 mA $cm^{-2}$ at 4.50 V $\mu m^{-1}$), and an excellent field emission stability over 480 min.[283] The enhanced field emission performance was due to the increased conductivity and decreased work function of the hydrogenated $TiO_2$ nanotubes.[283]

**6.1.6. Microwave Absorption.** Gigahertz radar microwave absorption materials play important roles in many civil and military applications.[284−291] Ferroelectric ceramics and carbonaceous materials are the traditional candidates.[284−292] However, ceramic ferroelectrics cannot be used as such because


dx.doi.org/10.1021/cr400624r | Chem. Rev. 2014, 114, 9890−9918

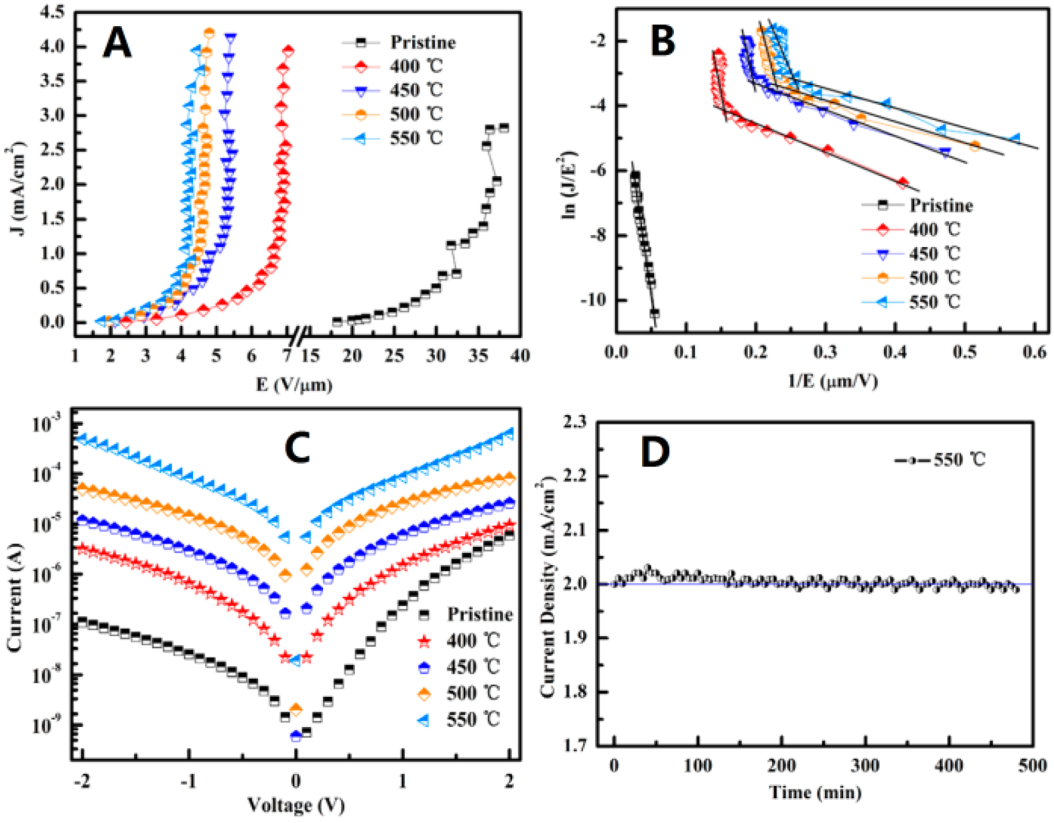


**Figure 20.** (A) *J*–*E* curves, (B) Fowler–Nordheim, and (C) *I*–*V* characteristics plots of pristine and hydrogenated $TiO_2$ nanotubes. (D) Field emission stability from H:TNAs obtained at 550 °C at a constant electric field of 4.23 V $\mu m^{-1}$. Straight line is a guiding line for the viewer.[283] (Reprinted with permission from ref 283. Copyright 2012 IOP Publishing Ltd.)

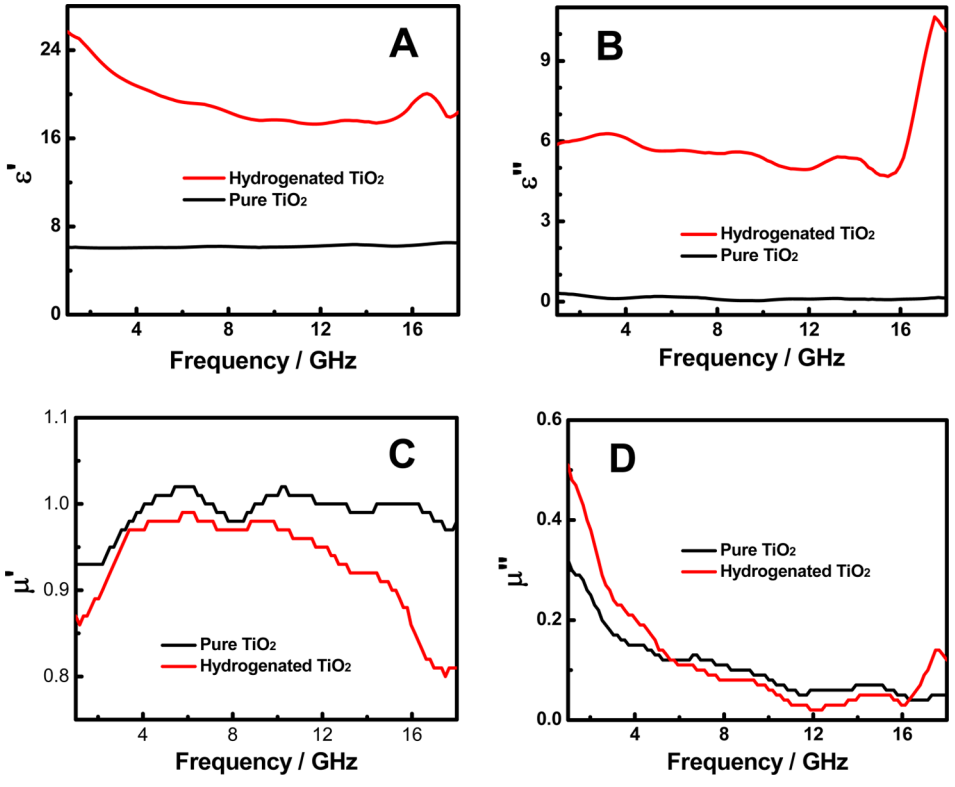


**Figure 21.** (A) $\varepsilon'$ and (B) $\varepsilon''$ and (C) $\mu'$ and (D) $\mu''$ of pure anatase and hydrogenated $TiO_2$ nanocrystals.[295] (Reprinted with permission from ref 295. Copyright 2013 WILEY-VCH Verlag GmbH & Co. KGaA, Weinheim.)


dx.doi.org/10.1021/cr400624r | *Chem. Rev.* 2014, 114, 9890–9918

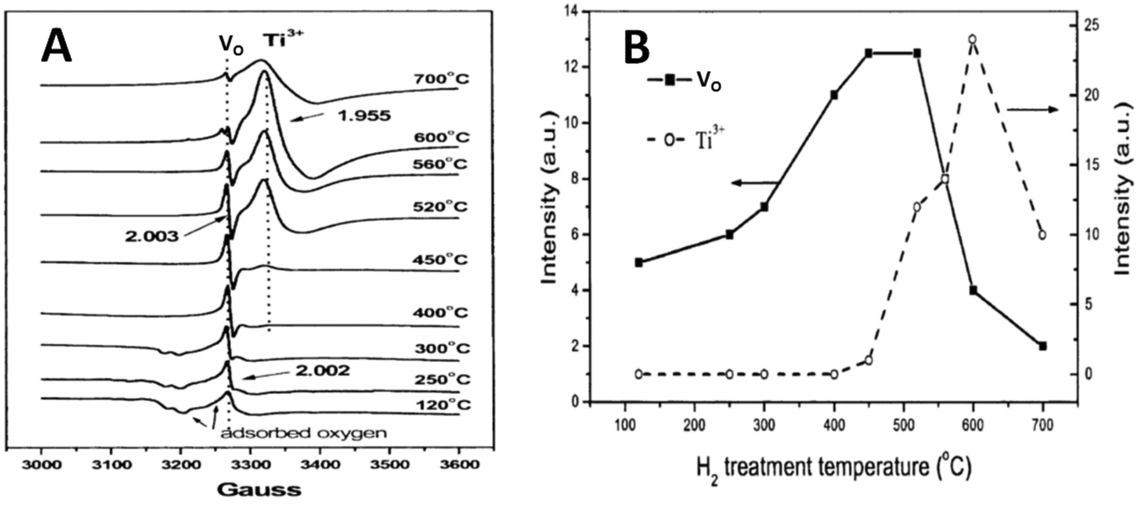


**Figure 22.** (A) ESR spectra of $V_O$ and $Ti^{3+}$ and (B) ESR intensity of $V_O$ and $Ti^{3+}$ as a function of $H_2$ treatment temperature.[242] (Reprinted with permission from ref 242. Copyright 2002 Elsevier Science Ltd.)

of the large reflection at their interfaces with air.[292] $TiO_2$ is traditionally not a good microwave absorption material, due to its low absorption in the gigahertz region.[127,128,293,294] Xia et al. has recently shown that hydrogenated $TiO_2$ nanocrystals displayed excellent microwave absorption performance.[295] Complex permittivity and permeability values are used to evaluate the microwave absorption properties.[284−294,296] The real and imaginary parts of permittivity, $\varepsilon'$ and $\varepsilon''$, are related to the stored and dissipated electrical energy within the medium. Their ratio, $tg\delta_\varepsilon = \varepsilon''/\varepsilon'$, is called the magnetic dissipation factor, indicating the ratio of the lost electrical energy over stored.[284−294,296] Similarly, the real and imaginary part of permeability, $\mu'$ and $\mu''$, are related to the stored and dissipated magnetic energy within the medium. Their ratio, $tg\delta_\mu = \mu''/\mu'$, is called the magnetic dissipation factor, indicating the ratio of the lost magnetic energy over stored energy.[284−294,296] The hydrogenated $TiO_2$ nanocrystals/epoxy composites displayed larger $\varepsilon'$ values in the frequency range 1.0−18.0 GHz (Figure 21A): decreasing gradually from 25.7 at 1.0 GHz to 17.7 at 10.0 GHz. Their $\varepsilon'$ average value was about 4.3 times of the pure $TiO_2$ nanocrystals (6.1−6.5).[295] Their $\varepsilon''$ value (5.9−10.6) was larger than that of $TiO_2$ nanocrystals/epoxy composites (0.03−0.3) as well (Figure 21B), around 70 times improvement.[295] Their $tg\delta_\varepsilon$ value was 15 times bigger.[295] Their $\mu'$ value (Figure 21C) was slightly smaller, and the $\mu''$ value behaved differently (Figure 21D).[295] Recently, they also reported that the microwave absorption performance could be tuned by controlling the hydrogenation conditions.[297]

## 6.2. Debates on the Fundamental Properties

**6.2.1. Structural Disorder.** Chen et al. observed a clearly seen disordered surface layer of the hydrogenated $TiO_2$ nanocrystals from the hydrogenation process with HRTEM.[102] Naldoni et al. confirmed formation of a crystalline/disordered core/shell structure of hydrogenated $TiO_2$ nanocrystals in a comparative HRTEM study, and they also revealed that there was a lattice contraction induced by the existence of $V_O$.[298] A clear crystalline-disordered core−shell structure was also observed for the hydrogenated $TiO_2$ nanocrystals obtained by treating the commercial Degussa P25 under 35 bar hydrogen and room temperature up to 20 days in the study by Lu et al.[254] Naldoni et al. believed the narrow band gap (1.85 eV) of their hydrogenated black $TiO_2$ nanocrystals was due to the coeffects of oxygen vacancies and surface disorder.[298] Xia and Chen also confirmed the lattice contraction of the hydrogenated $TiO_2$ nanocrystals.[244] Jiang et al. found the lattice distortion during hydrogenation through HRTEM observations fast Fourier transform analysis.[299] Zheng et al. found that the Raman spectral-broadening hydrogenated $TiO_2$ nanowire microspheres were most likely from the disorder or destruction of the crystal lattice.[247] Wang and Xu et al. found that the (101) diffraction peak of hydrogenated $TiO_2$ nanosheets slightly shifted toward a higher diffraction angle, indicating a smaller interplanar crystal spacing and structural changes during the hydrogenation process.[248] Wang and Jiang et al. observed that the hydrogenated black $TiO_2$ nanocrystals had crystalline core/amorphous shell structures.[249] Lu and Zhou et al. revealed that the hydrogenated $TiO_2$ nanotube had a very clear surface, while there was an obvious amorphous layer on the outside surface of the untreated nanotube.[276] They attributed the discrepancy in the structural change in the hydrogenation with the observation in other studies as mainly due to the different hydrogenation conditions.[276] Li et al. found there was a weak lattice expansion because of the oxygen vacancies induced by the hydrogenation treatment.[277] Wang et al. also reported a crystalline core−amorphous shell structure ($TiO_2$@$TiO_{2-x}$) of black $TiO_2$ nanocrystals obtained by reducing with aluminum, which displayed visible and infrared absorption, enhanced photocatalytic, solar thermal, and photoelectrochemical properties.[300]

**6.2.2. $Ti^{3+}$.** Liu et al. performed in situ electron spin resonance (ESR) measurements of $V_O$ and $Ti^{3+}$ in the hydrogenation of anatase $TiO_2$ nanoparticles (Figure 22).[242] When hydrogenated below 300 °C, $V_O$ ($g$ = 2.002) and surface-adsorbed superoxide radical ($g$ = 2.003) were observed.[242] $Ti^{3+}$ started to show up at 450 °C, and its magnitude increased with further temperature increase, accompanied by the decrease of $V_O$ content.[242] At 700 °C, both $Ti^{3+}$ and $V_O$ concentration decreased and the phase changed to rutile from anatase.[242]

Chen et al. reported that $Ti^{3+}$ ions were not detected in hydrogenated black $TiO_2$ nanocrystals with conventional XPS.[102] Later, with synchrotron X-ray absorption, emission, and photoelectron spectroscopies they further confirmed the absence of $Ti^{3+}$ ions in hydrogenated black $TiO_2$ nano-


dx.doi.org/10.1021/cr400624r | Chem. Rev. 2014, 114, 9890−9918

particles.[243] Similarly, Wang and Li et al. found that the Ti 2p XPS spectra of pure and hydrogenated $TiO_2$ nanowires treated at 450 °C were identical, confirming the typical characteristics of $Ti^{4+}$ and absence of $Ti^{3+}$ in the hydrogenated $TiO_2$ nanowires.[246] Likewise, identical Ti 2p XPS features were found for hydrogenated and pure $TiO_2$ nanotubes by Zhang et al.[282] and Naldoni et al.[298] independently. Wang and Jiang et al. found the absence of ESR signals of $Ti^{3+}$ ($g$ = 1.957), indicating the absence of $Ti^{3+}$ in hydrogenated $TiO_2$ obtained by hydrogen plasma, besides their almost identical Ti 2p XPS spectra.[249] However, Wang and Xu et al. found that the Ti 2p XPS peak of hydrogenated $TiO_2$ nanosheets had a shift toward lower binding energy with a detectable shoulder ascribed to $Ti^{3+}$.[248] Lu et al. found XPS signals for the presence of $Ti^{3+}$ species after the hydrogenated $TiO_2$ surface was cleaned for 1 min and concluded that annealing under $H_2$ produced $Ti^{3+}$ species inside the lattices instead of on the surface.[276] Lu et al. found there were two extra peaks centered at around 457.9 and 463.5 eV in the Ti 2p XPS spectrum of hydrogenated $TiO_2$ nanotubes and attributed them to the Ti 2p3/2 and Ti 2p1/2 peaks of $Ti^{3+}$ ions in the hydrogenated $TiO_2$ nanotubes.[281] Similarly, Jiang et al. suggested that the peaks at 457.6 and 463.3 eV in the Ti 2p XPS spectrum of hydrogenated $TiO_2$ nanocrystals were due to the Ti 2p3/2 and for Ti 2p1/2 levels of $Ti^{3+}$ ions.[299] Meanwhile, Naldoni et al. suggested the absence of the superoxide ($O^{2-}$) radical signal and the presence of $Ti^{3+}$ centers were in the bulk of hydrogenated $TiO_2$ nanocrystals instead of on the surface as seen from their electroparamagnetic resonance results.[298] Yu et al. found that the distribution and concentration of oxygen vacancy and $Ti^{3+}$ defects were largely influenced by the hydrogenation condition (e.g., temperature and time; Figure 23).[253] The trend of these defect changes against hydrogenation temperature was apparently different from what Liu reported earlier (Figure 22).[242]

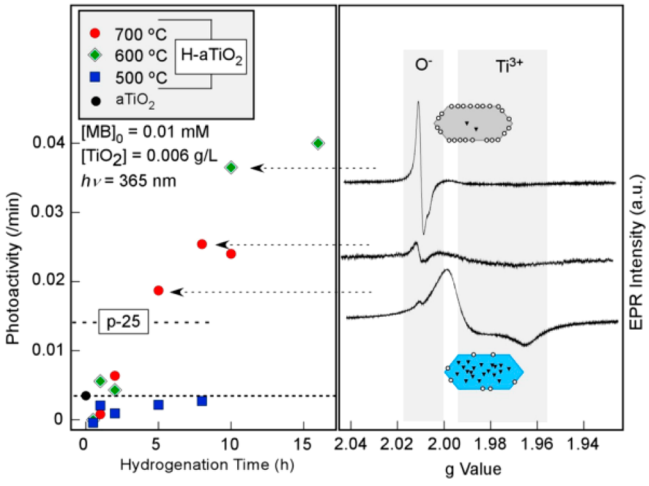


**Figure 23.** Photoactivities and EPR spectra of H-a$TiO_2$.[253] (Reprinted with permission from ref 253. Copyright 2013 American Chemical Society.)

**6.2.3. Ti−H.** Zheng et al. found that hydrogenated $TiO_2$ nanowire microspheres exhibited one shoulder peak at the lower binding energy side of the broader Ti 2p peak and attributed it to the surface Ti−H bonds formed under hydrogen atmosphere.[247] Formation of surface Ti−H bonds occurred at the expense of surface Ti−OH bonds, hence decreasing the number of surface OH groups in $TiO_2$.[247] Wang and Xu et al. believed that the surface of hydrogenated $TiO_2$ nanosheets was fully covered with the Ti−H and O−H chemical bonds, accompanied by $Ti^{3+}$ and oxygen vacancies.[248] They suggested that the {001} facets of hydrogenated $TiO_2$ nanosheets were maintained by Ti−H chemical bond formation, resulting in the change from $Ti_{5c}$ to $Ti_{6c}$.[248] Wang and Jiang et al. attributed the peak at 457.1 eV in the Ti 2p XPS spectrum of hydrogenated $TiO_2$ nanocrystals to surface Ti−H bonds.[249] Zhang et al. suggested the peak at approximately 59.28° in the XRD pattern of hydrogenated $TiO_2$ nanotubes, which shifted to 59.58° from 59.18° with increased treating temperature, was caused by formation of a Ti−H bond.[282]

**6.2.4. Ti−OH.** Wang and Li et al. found that the hydrogenated $TiO_2$ nanowires had a shoulder peak at the higher binding energy side besides the main XPS O 1s peak and attributed it to the formation of a hydroxyl group Ti−OH.[246] In the O 1s core-level XPS spectra of hydrogenated $TiO_2$ nanotubes Lu and Li et al. attributed the peaks centered at 532.0 and 531.4 eV to Ti−OH groups (Figure 24A).[281] A similar increased Ti−OH XPS feature for hydrogenated $TiO_2$ nanotubes was found by Zhang et al.[282] Lu and Zhou et al. observed similar O 1s XPS spectra of the hydrogenated $TiO_2$ nanotube arrays after cleaning the surface with an electron beam and concluded that little effect was caused by the hydrogenation treatment on the O 1s spectra (Figure 24B).[276]

Harris et al. found that when rutile was heated in hydrogen the presence of hydrogen in the crystal was indicated with the OH absorption peaks at 3276 $cm^{-1}$ due to the H bonded between two lattice O atoms and at 3323 $cm^{-1}$ due to H bonded to a single lattice O atom.[234] Hydrogen reduction at higher temperatures resulted in the production of both OH groups and oxygen vacancies with the attendant crystal disorder.[234] Zheng et al. found similar results in that for hydrogenated $TiO_2$ the intensity of the OH peak in the Fourier transform infrared (FTIR) spectrum was much lower than pure $TiO_2$.[247] However, Wang and Xu et al. found more surface OH groups on hydrogenated $TiO_2$ nanosheets.[248] Wang and Jiang et al. found that both hydrogenated and pristine $TiO_2$ had OH absorption bands around 3400 and 1635 $cm^{-1}$.[249] Hydrogenated $TiO_2$ displayed extra peaks at 3685, 3670, and 3645 $cm^{-1}$ due to tetrahedral coordinated vacancies $Ti^{4+}$−OH and at 3710 $cm^{-1}$ due to embedded terminal OH groups (Figure 25A and 25B).[249] Lu and Zhou et al. found that less adsorbed water and/or hydroxyl groups present hydrogenated $TiO_2$ nanotubes based on the weaker bands at 3446 and 1645 $cm^{-1}$.[276] Chen et al. reported that both hydrogenated and pristine $TiO_2$ nanocrystals had similar infrared OH bands around 3400 $cm^{-1}$ from bridging OH groups and around 3700 $cm^{-1}$ from the stretching and wagging of O−H vibrations (Figure 25C).[243] The decreased intensity of the terminal O−H mode after hydrogenation suggested that the O dangling bonds were not passivated with the hydrogen incorporated into the $TiO_2$.[243] The surface-disordered black $TiO_2$ had a broader OH absorption band, suggesting a more varied environment for the OH groups than the white $TiO_2$.[243] Xia et al. found no OH absorption bands in hydrogenated $TiO_2$ nanocrystals (Figure 25D), while the pure $TiO_2$ nanocrystals had apparent OH bands.[295]

Wang and Jiang et al. observed a higher peak at 5.5 ppm in the $^1H$ nuclear magnetic resonance (NMR) spectra in the hydrogenated $TiO_2$ nanocrystals from bridging hydroxyl groups and extra signals at 0.01 and 0.4 ppm from the internal and terminal hydroxyl groups in the surface disordered layer as a


dx.doi.org/10.1021/cr400624r | Chem. Rev. 2014, 114, 9890−9918

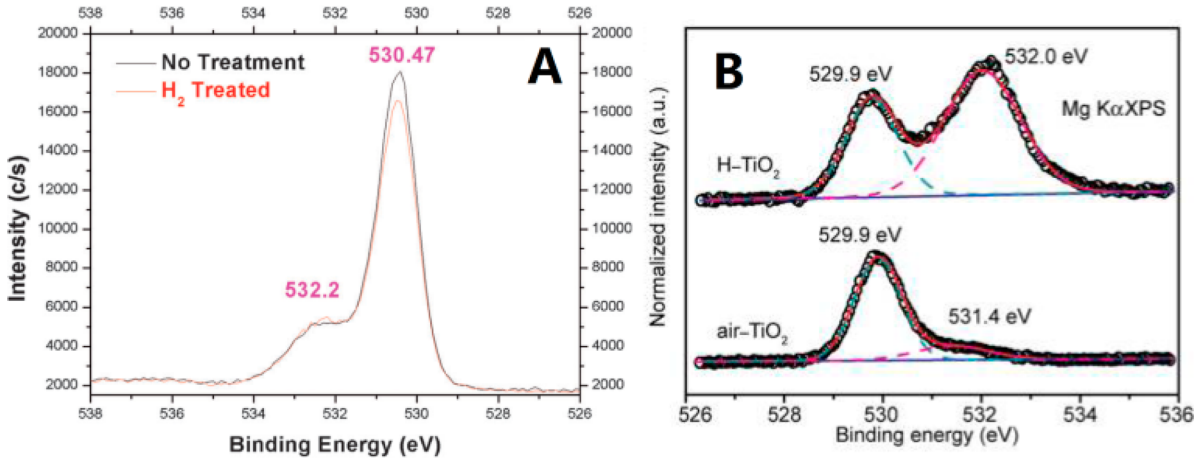


**Figure 24.** (A) High-resolution O 1s XPS of the $TiO_2$ nanotube arrays with and without $H_2$ treatment.[276] (Reprinted with permission from ref 276. Copyright 2012 Wiley-VCH Verlag GmbH & Co. KGaA, Weinheim.) (B) Normalized O 1s core-level XPS spectra of air-annealed (air-$TiO_2$) and hydrogenated (H-$TiO_2$) $TiO_2$ nanotubes.[281] (Reprinted with permission from ref 281. Copyright 2012 American Chemical Society.)

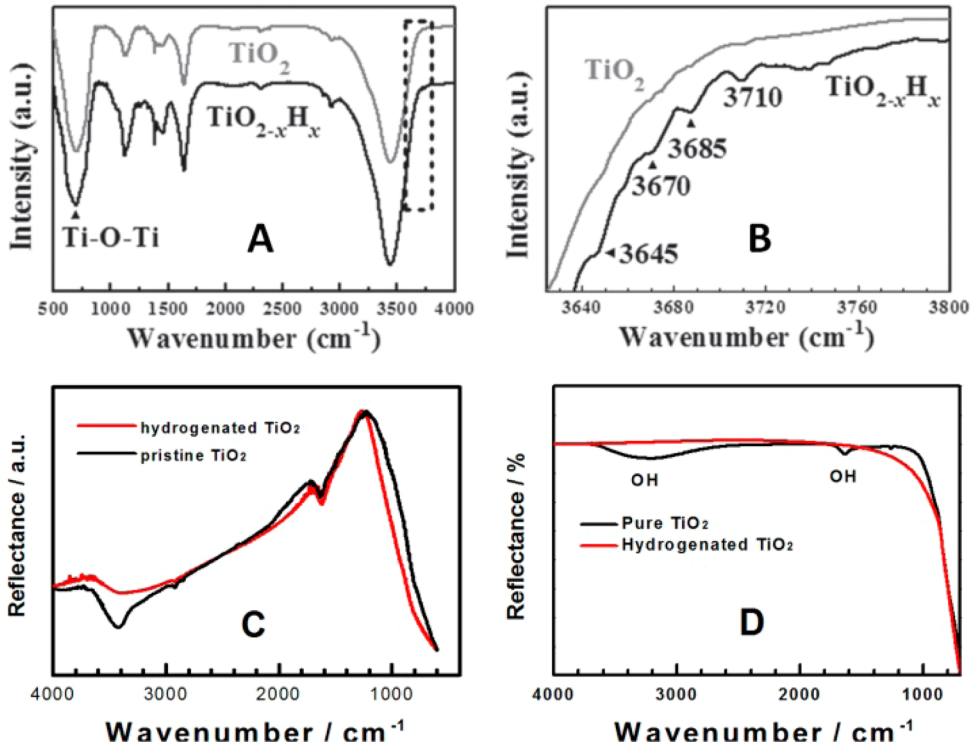


**Figure 25.** (A and B) FTIR spectra of pristine $TiO_2$ and $TiO_{2-x}H_x$ reported by Wang et al.[249] (Reprinted with permission from ref 249. Copyright 2013 WILEY-VCH Verlag GmbH & Co. KGaA, Weinheim.) (C) FTIR spectra of pristine $TiO_2$ and $TiO_{2-x}H_x$ reported by Chen et al.[243] (Reprinted with permission from ref 243. Copyright 2013 Nature Publishing Group.) (D) FTIR spectra of pristine and hydrogenated $TiO_2$ nanocrystals reported by Xia et al.[295] (Reprinted with permission from ref 295. Copyright 2013 WILEY-VCH Verlag GmbH & Co. KGaA, Weinheim.)

result of hydrogenation (Figure 26A and 26B).[249] Chen et al. found that hydrogenated black $TiO_2$ nanocrystals showed a slightly broader peak at chemical shift +5.7 ppm than pristine $TiO_2$ nanocrystals.[243] They attributed this difference to hydrogen incorporation at various bridging sites in the disordered phases or on the facets.[243] They also found that hydrogenated $TiO_2$ nanocrystals had two additional small and narrow peaks at chemical shifts of −0.03 and 0.73 ppm compared to pristine $TiO_2$ nanocrystals, indicating the low hydrogen concentration and the dynamic exchange nature between hydrogen in the different environments in hydrogenated $TiO_2$ nanocrystals.[243] Xia et al. found that hydrogenated $TiO_2$ nanocrystals had much smaller OH signals than the pure $TiO_2$ nanocrystals in their NMR spectra (Figure 26D).[295]

**6.2.5. Oxygen Vacancy.** Khader et al. investigated the electrical conductivity of rutile $TiO_2$ to study the hydrogen reduction mechanism between 300 and 500 °C.[238] They suggested that the reduction led to oxygen loss and oxygen vacancy formation

$$TiO_2 + xH_2(g) \rightarrow TiO_{2-x} + xH_2O(g) \quad (6)$$

$$O^{2-}(s) + H_2(g) \rightarrow H_2O(g) + V_r^{2-} \quad (7)$$


dx.doi.org/10.1021/cr400624r | Chem. Rev. 2014, 114, 9890−9918

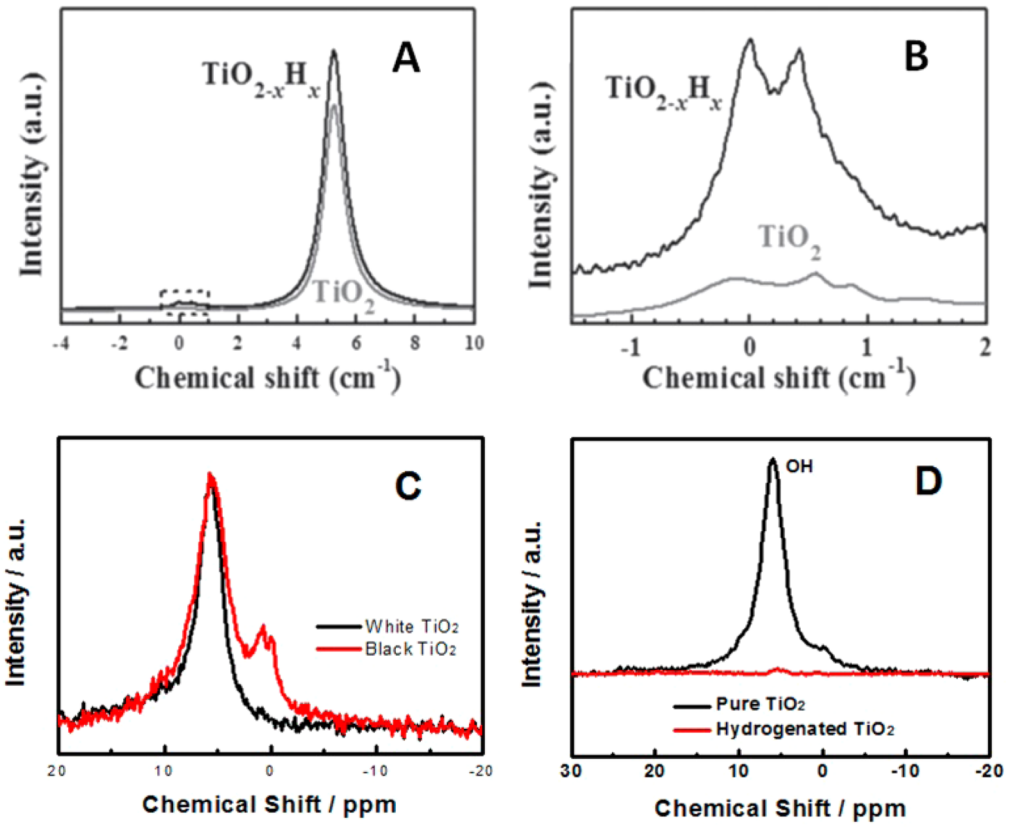


**Figure 26.** (A and B) $^1$H NMR spectra of pristine $TiO_2$ and $TiO_{2-x}H_x$ reported by Wang et al.[249] (Reprinted with permission from ref 249. Copyright 2013 WILEY-VCH Verlag GmbH & Co. KGaA, Weinheim.) (C) $^1$H NMR spectra of pristine $TiO_2$ and $TiO_{2-x}H_x$ reported by Chen et al.[243] (Reprinted with permission from ref 243. Copyright 2013 Nature Publishing Group.) (D) $^1$H NMR spectra of pristine and hydrogenated $TiO_2$ nanocrystals reported by Xia et al.[295] (Reprinted with permission from ref 295. Copyright 2013 WILEY-VCH Verlag GmbH & Co. KGaA, Weinheim.)

where $V_r^{2-}$ is a reactive $V_O$.[238] The fresh oxygen vacancies produced were the active sites for $H_2$ adsorption, acted as defects in the crystal lattice, and enhanced its conductivity, because the accompanying electrons moved to the conduction band.[238] As a result, the point defect formation led to the gradual conductivity increase of rutile with the reduction time (Figure 27).[238] This process included three steps: (1) hydrogen adsorption on the defects; (2) $O^{2-}$ ion reduction on the surface; and (3) oxygen diffusion outward.[238] Rekoske et al. reported that reduction of anatase and rutile $TiO_2$ with $H_2$ started from 573 K.[240] The initial reduction rate was small due to the limited number of available surface H atoms and then was accelerated when more sites were produced for $H_2$ dissociation.[240] The reduction rate became independent of the reduction time as the surface H concentration increased to the similar consumption rate of surface O.[240] The reduction rate slowed as the surface O supply diminished, until eventually dictated by the O-atom diffusion to the surface from the lower layers.[240]

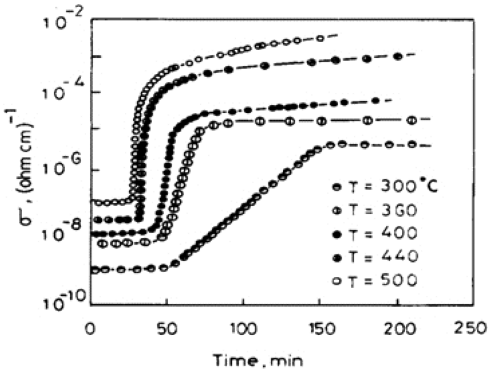


**Figure 27.** Change of the electrical conductivity, $\sigma$, of the rutile pellets with reduction time.[238] (Reprinted with permission from ref 238. Copyright 1993 American Chemical Society.)

Haerudin et al. found that formation of oxygen vacancies occurred on $TiO_2$–P25's surface by reduction with dry hydrogen, and water vapor accelerated their formation.[241] The density of surface vacancies reached saturation upon hydrogen treatment above 400 °C, and the vacancies in the bulk were then formed.[241] Electrons were delocalized in the bulk and occupied the conduction band, causing decreased IR transmittance and increased electrical conductivity.[241] The number of vacancies was found to be related to the IR absorbance at 1900 $cm^{-1}$.[241] They found a reaction enthalpy of 183 kJ $mol^{-1}$ for the formation of vacancies by hydrogen reduction.[241] Onishi found the activation energy was 121 kJ $mol^{-1}$ for oxidizing hydrogen on anatase.[301]

Wang and Li et al. believed that a high density of oxygen vacancies was created in hydrogenated $TiO_2$ nanowires, served as electron donors in absorbing visible light, and improved the photocatalytic activity.[246] Wang et al. found that pure $TiO_2$ nanosheets had a strong ESR signal with $g$ values of 1.992 and 1.962, as typical for the $Ti^{3+}$ center, originating from substitution of $O^{2-}$ ions by the $F^-$ ions, but had no other


dx.doi.org/10.1021/cr400624r | Chem. Rev. 2014, 114, 9890–9918

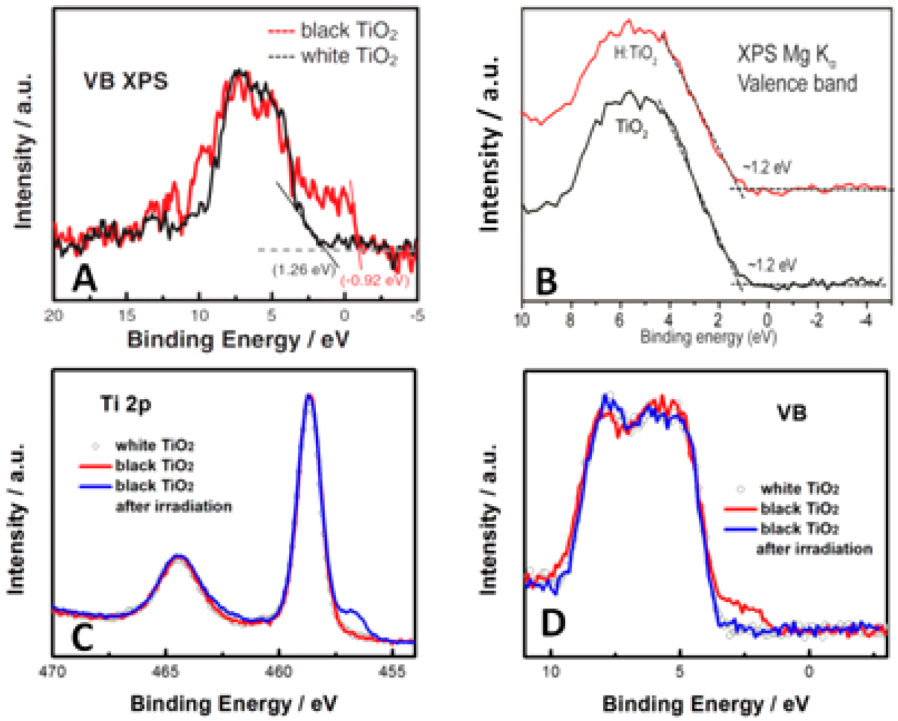


**Figure 28.** (A) Valence-band XPS spectra of the white and black $TiO_2$ nanocrystals.[102] (Reprinted with permission from ref 102. Copyright 2011 The American Association for the Advancement of Science.) (B) XPS valence-band spectra of the pristine $TiO_2$ and hydrogenated H:$TiO_2$ nanowires. Dashed lines highlight the linear extrapolation of the curves, deriving a band edge position of ~1.2 eV.[246] (Reprinted with permission from ref 246. Copyright 2011 American Chemical Society.) (C) Synchrotron Ti 2p and (D) VB XPS spectra of white and black $TiO_2$ before and after 3 h of 635 eV X-ray illumination.[243] (Reprinted with permission from ref 243. Copyright 2013 Nature Publishing Group.)

signal, such as $O_2$ or $O^{2-}$.[248] On the other hand, hydrogenated $TiO_2$ nanosheets gave a very different and stronger ESR signal of the $Ti^{3+}$ and $O^-$.[248] Jiang et al. found that $Ti^{3+}-V_O$ associates, vacancy clusters, and voids of vacancy associates were produced in hydrogenated $TiO_2$ nanocrystals based on a positron annihilation lifetime spectroscopy study.[299]

Li et al. found in hydrogenated $TiO_2$ nanotubes (H-TNTs) oxygen vacancies were shallow donors and increased the electronic conductivity and photoelectrocatalytic performance.[302] Pesci et al. examined the oxygen-deficient H:$TiO_2$ nanotube arrays with transient absorption spectroscopy and suggested that with a small external bias the improved electrical properties allowed effective fast spatial separation of electron–hole pairs which suppressed charge carrier recombination and enhanced the activity.[303]

**6.2.6. Valence-Band Edge.** Chen et al. attributed the black color of the hydrogenated $TiO_2$ nanoparticles to the valence-band shift, evidenced from valence-band XPS measurement (Figure 28A).[102] Naldoni et al. also confirmed the valence band shift of hydrogenated $TiO_2$ nanocrystals independently.[298] They found that both the valence band and the band tail blue shifted in the hydrogenated $TiO_2$ nanocrystals toward the vacuum level compared to the band edge of pristine $TiO_2$ nanocrystals.[298] However, Wang and Li et al. revealed that pure and hydrogenated $TiO_2$ nanowires had similar valence-band structures, suggesting that the valence-band position was barely influenced by the hydrogen treatment (Figure 28B).[246] A similar observation was obtained on hydrogenated $TiO_2$ nanosheets.[248,249] Lu et al. found that although the valence band XPS spectra were very similar for hydrogenated and pure $TiO_2$ nanotubes, differences in the valence-band spectra were observed after surface cleaning in that the valence-band edge of hydrogenated $TiO_2$ nanotubes shifted slightly toward the band gap, indicating slight narrowing of the band gap by the hydrogenation modification, which they attributed to the oxygen vacancies inside.[276] Chen et al. recently reported that $Ti^{3+}$ ions did not contribute to extra band-gap states of the hydrogenated $TiO_2$ nanocrystals.[243] They found that when $Ti^{3+}$ showed up, the midgap states disappeared.[243] They measured the Ti 2p XPS and valence-band XPS changes before and after shining an X-ray beam for an extended time.[243] Before X-ray irradiation, hydrogenated and pristine $TiO_2$ nanocrystals displayed almost identical Ti 2p XPS spectra and the hydrogenated $TiO_2$ exhibited additional midgap states.[243] After 3 h X-ray irradiation a peak appeared at 457.0 eV in the Ti 2p XPS spectrum of hydrogenated $TiO_2$ nanocrystals, which was a typical characteristic of $Ti^{3+}$ species, and simultaneously the midgap states disappeared, resulting in almost identical valence-band XPS spectra of the black and white $TiO_2$ nanocrystals (Figure 28C and 28D).[243]

**6.2.7. Stability.** Chen et al. found that the hydrogenated black $TiO_2$ nanocrystals exhibited substantial stability during the photocatalytic hydrogen generation from water under sunlight.[102] Throughout the 22-day testing period the black $TiO_2$ nanocrystals exhibited persistent high $H_2$ production capability under the full spectrum solar irradiation when loaded with 0.6 wt % Pt in a 1:1 water–methanol solution.[102] By heating amorphous $TiO_2$ under $H_2$ stream Naldoni et al. obtained black $TiO_2$ powder that was stable over 10 months in air.[298] Yu et al. synthesized different color anatase $TiO_2$ nanocrystals, which were blue after shorter hydrogenation and gray after longer hydrogenation treatments.[253] The color did not change after several months' storage under ambient environments.[253] Li et al. reported their electrochemically


dx.doi.org/10.1021/cr400624r | Chem. Rev. 2014, 114, 9890–9918

hydrogen-modified anatase displayed good stability in their highly improved supercapacitor testing.[256] Their doped black $TiO_2$ was claimed highly stable with the beneficial effects persisting for over 1 year and possessed a significantly narrower band gap and higher conductivity.[256] Danon et al. claimed that formation of black $TiO_2$ nanotubes depended on the reaction vessel's material.[252] In a stainless steel reactor, the nanotubes' color was black; in a quartz reactor, the color was blue, which turned white when exposed to air.[252]

It may be meaningful to note that the stability of the hydrogenated $TiO_2$ nanocrystals can be damaged by high-energy irradiations, such as X-ray. Chen et al. observed that upon 3 h X-ray irradiation the black $TiO_2$ nanocrystals lost their characteristic XPS features and had almost the same valence-band XPS results as white $TiO_2$ nanoparticles.[243]

**6.2.8. Theoretical Models.** Chen et al. found that in hydrogenated $TiO_2$ nanocrystals midgap states and a reduced band gap were obtained with hydrogenated lattice disorders.[102] In their disordered $TiO_2$ nanocrystal model H atoms were bonded to O and Ti atoms.[102] Two groups of midgap states were predicted at about 3.0 and 1.8 eV, respectively.[102] The higher energy group was only made of Ti 3d orbitals.[102] The lower energy group was mixed O 2p and Ti 3d orbitals.[102] The hydrogen 1s orbital contributed little to either group but stabilized the lattice disorders by passivating their dangling bonds.[102] Lattice disorders contributed to the midgap states and the Fermi level located below 2.0 eV.[102]

Lu et al. investigated the hydrogenation effect on the structure and photocatalytic properties of anatase $TiO_2$ (101) and (001) surfaces with DFT-PBE calculations.[304] They proposed that the high photoactivity of disorder-engineered $TiO_2$ nanocrystals was ascribed to surface effects (Figure 29).[304] They found that hydrogen atoms were chemically absorbed on both $Ti_{5c}$ and $O_{2c}$ atoms for (101), (001), and (100) surfaces by taking into account the synergistic effect of Ti−H and O−H bonds.[304] They suggested that the hydrogenation-induced lattice distortions on (101) and (100) surfaces of nanoparticles enhanced the intraband coupling within the valence band, while the (001) surface was not largely affected.[304] They indicated that the adatoms not only induced the lattice disorders but also interacted strongly with the O 2p and Ti 3d states, resulting in a considerable contribution to the midgap states.[304] They found the optical absorption was dramatically red shifted due to the midgap states and the photogenerated electron−hole separation was substantially promoted as a result of electron−hole flow between different facets of hydrogenated nanoparticles.[304] This accounted for the exceptionally high-energy conversion efficiency of black $TiO_2$ under solar irradiation.[304] Moreover, they found that hydrogenation reversed the redox behavior of different surfaces of nanoparticles and therefore proposed that one could tune the photoexcited electron−hole flow between different surfaces of nanoparticles in accordance to one's request by appropriate chemical surface treatment.[304]

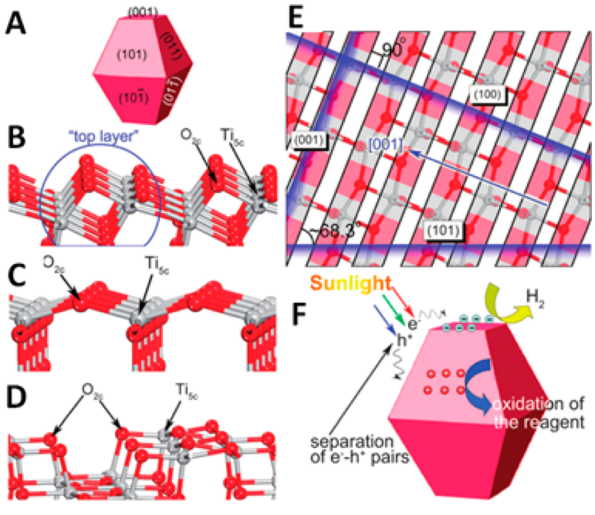


**Figure 29.** (A) Schematic drawings of anatase $TiO_2$ nanoparticles grown in acidic solution. (B, C, and D) Relaxed surfaces of the clean (101), (001), and (100) facets, respectively. (E) Illustration of the layered structure (s-layer) of anatase $TiO_2$ and the (101), (001), and (100) facets sloping, parallel, and perpendicular to the s-layers, respectively; the arrow in E denotes the soft axes lying along the [001] direction. (F) Spatial separation of the photogenerated electron−hole pairs as a result of electron−hole flow between the hydrogenated (101) and (001) facets.[304] (Reprinted with permission from ref 304. Copyright 2011 The Owner Societies.)

Liu et al. pointed out that hydrogenated black $TiO_2$ required not only hydrogen passivation of Ti and O dangling bonds on the surface.[80] With the DFT-PBE and hybrid functional calculations they investigated hydrogen's role in creating lattice disorders in the nanocrystals.[80] They examined the effects of lattice distortion on the electronic energy bands upon using a 2 × 2 × 1 supercell with the formula $Ti_{16}O_{32}$ (Figure 30A).[80]

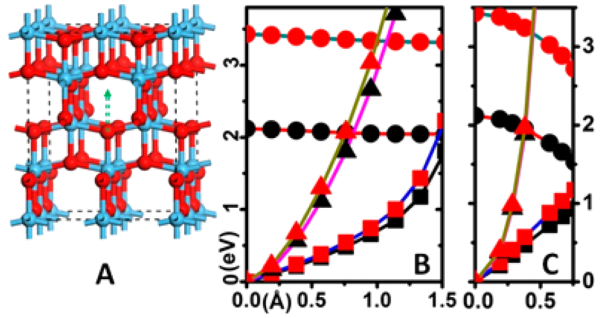


**Figure 30.** (a) 2 × 2 × 1 anatase supercell, where the sky blue and red balls represent Ti and O atoms, respectively. Variations of VBM (represented by squares), CBM (circles), and total energy (triangles) calculated by PBE (black) and the hybrid functional (red) as a function of the distortion of (b) the O sublattice and (c) the Ti sublattice.[80] (Reprinted with permission from ref 80. Copyright 2013 American Physical Society.)

They found that (Figure 30B) the CBM did not change upon O-sublattice distortion but red shifted upon Ti-sublattice distortion; the VBM blue shifted in either case (Figure 30C).[80] The small effect of the O distortion upon CBM was attributed to the nature of the Ti 3d orbital featured CBM.[80] The lattice disorder was mainly due to the O distortion.[80] Hydrogenation played an important role in reducing the distortion energy in raising the VBM.[80,102]

They examined further the hydrogenation effect by comparing two bulk anatase models, either with an interstitial $H_2$ molecule or with two H atoms bonded to O and Ti separately.[80] The CBM electrons were not sensitive to local lattice distortions nor to H-bonding-induced changes.[80] The midgap states changed upon both lattice distortion and H bonding.[80] The enhanced photocatalytic efficiency was due to the different spatial extent of the conduction electron and


dx.doi.org/10.1021/cr400624r | Chem. Rev. 2014, 114, 9890−9918

midgap hole states which separated the photoexcited electrons and holes.[80] The lattice distortion caused by H in bulk anatase was not the most stable and might release hydrogen from the lattice even at room temperature.[80]

Pan et al. investigated the effects of H doping on the electronic properties of three $TiO_2$ polymorphs—anatase, rutile, and brookite.[261] They suggested that incorporation of hydrogen, interstitially or substitutionally, was important for n-type $TiO_2$ formation.[261] Interstitial hydrogen caused band-gap narrowing, while substitutional hydrogen did not reduce the band gap of anatase.[261] (H, N)-*co*-Doping narrowed the band gap and improved the photocatalytic performance of anatase and brookite $TiO_2$ with more absorption in visible light but had little effect on rutile $TiO_2$.[261]

## 7. CONSIDERATION OF ELEMENTARY DEFECTS IN SELF-STRUCTURAL MODIFICATIONS

The correlation between the defect constitution of solids and their catalytic activity was widely accepted as a formal basis to explain the details of their catalytic process since 1949.[305] For $TiO_2$ it was demonstrated that the very pure stoichiometric $TiO_2$ was not an active catalyst for certain chemical syntheses.[305] In general, six kinds of native-point defects may exist in the $TiO_2$: the vacancies of titanium ($V_{Ti}$) and oxygen ($V_O$), the interstitials of titanium ($Ti_i$) and oxygen ($O_i$), and two antisite defects of $Ti_O$ and $O_{Ti}$. As $TiO_2$ is naturally reduced and n-type, $Ti_i$ and $V_O$ were usually proposed and resulted in the apparent oxygen deficiency ($O_d$) of $TiO_{2-x}$.[306−308] However, their exact roles in affecting the electronic structures of $TiO_2$ have not been completely understood.

### 7.1. Experimental Results

An oxygen-deficient rutile phase $TiO_{2-x}$ ($x < 0.008$) can be obtained under usual growth conditions.[309] The Magneli phase will be formed for larger values of $x$, whose structure may be regarded as consisting of an ordered array of planar defects.[310] In 1958, D. C. Cronemeyer studied rutile single crystals reduced with hydrogen at 700 °C and attributed the increased electrical conductivity to the ionization-trapped electrons in $V_O$.[311] Samples with electrical resistivity larger than 0.04 ohm·m displayed an optical absorption peak around 0.75 eV.[311] Samples with electrical resistivity less than 0.03 ohm·m had an optical absorption peak at 1.18 eV.[311] The shift of the absorption peak was attributed to the change of thermal activation energy with $V_O$ concentration.[311] J. H. Becker and W. R. Hosler found multiple-band conduction in n-type rutile at temperatures above 40 K.[312] Hasiguti et al. suggested the dominant defects for the electrical conductivity were mostly interstitial Ti ions in the $O_d$ range from $3.7 \times 10^{18}$ to $1.3 \times 10^{19}/cm^3$.[313,314]

Sekiya et al. found that oxidation or reduction controlled the color of the anatase single crystal that was annealed in hydrogen or oxygen atmosphere (Figure 31).[315] The as-grown crystal's color changed from pale blue through yellow to colorless when annealed in oxygen.[315] The color changed back to pale blue or dark blue when annealed in hydrogen.[315] The dark blue crystal turned dark green, yellow, and colorless after being heated in oxygen again.[315] Absorption spectra showed that the color came from the absorption bands located on the lower energy side rather than 2.5 eV or bands just below the fundamental absorption edge.[315] On the basis of the change in optical absorption depending on the annealing condition and

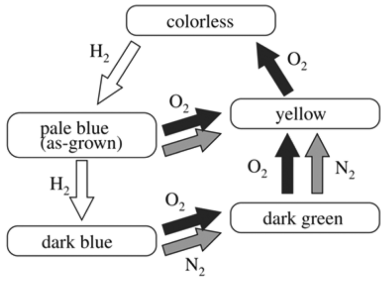


**Figure 31.** Change in characteristic color depending on the heat treatments, where white, gray, and black arrows represent heat treatments under hydrogen, inert, and oxygen atmospheres, respectively.[315] (Reprinted with permission from ref 315. Copyright 2004 The Physical Society of Japan.)

the results of the ESR measurement the authors proposed some models for these crystals containing various defects.[315] The colorless crystal was assumed to contain few defects.[315] In the pale blue crystal some hydrogen penetrating into the bulk resulted in hydroxyl group formation and supplied the conduction electrons.[315] The pale blue crystals were suggested to contain a few vacant oxygen sites.[315] In the dark blue and dark green crystals, some oxygen vacancies were indicated to coexist with the conduction electrons.[315] In the yellow crystal some electrons were trapped on the oxygen vacancies and absent in the conduction band at temperatures higher than 70 K.[315]

### 7.2. Theoretical Analysis

Due to the complexity of forming native defects in $TiO_2$ it is challenging to reveal a particular impurity's effect simply by measuring the doping-dependent photocatalytic process.[316] With the advantage of building ideal isolated defect models, theoretical results—especially those first-principles calculations—were expected to provide some instructive insights into the defect chemistry of $TiO_2$.[316]

Using a semiempirical self-consistent method, Yu et al. studied the electronic structure of point defects in reduced rutile.[317] They reported that the donor levels of oxygen vacancies and interstitial titanium were around 0.7 eV below the conduction band edge.[317] Using the GGA-PBE functional, He and Sinnott presented DFT calculations on the formation energies of Schottky (vacancy) and Frenkel (vacancy + interstitial) defects in rutile.[318] The Frenkel defect was easier to appear in rutile at low temperatures than the Schottky defect, and their formation enthalpy difference was about 1 eV.[318] Both Frenkel and Schottky defects preferred to form a cluster rather than to scatter.[318] Schottky and Frenkel had similar band features but with a smaller band gap than that of the defect-free structure.[318] Cho et al. found that the $V_O$ did not produce a defect level in the band gap, while the interstitial titanium generated a localized state 0.2 eV below the conduction band edge.[309]

Na-Phattalung et al. investigated the atomic structures and electronic properties of point defects in anatase (Figure 32).[316] They found that $Ti_i$ was a low-formation-energy quadruple donor and caused n-type conductivity.[316] $V_O$ had a higher formation energy and a lower kinetic energy to be created from perfect crystal.[316] Postgrowth formation of $V_O$ was possible by heating the sample for some time.[316] $O_i$ bonded to lattice oxygen impulsively to form an electrically inactive $O_2$ dimer, and antisite defects had high formation energies to automati-


dx.doi.org/10.1021/cr400624r | Chem. Rev. 2014, 114, 9890−9918

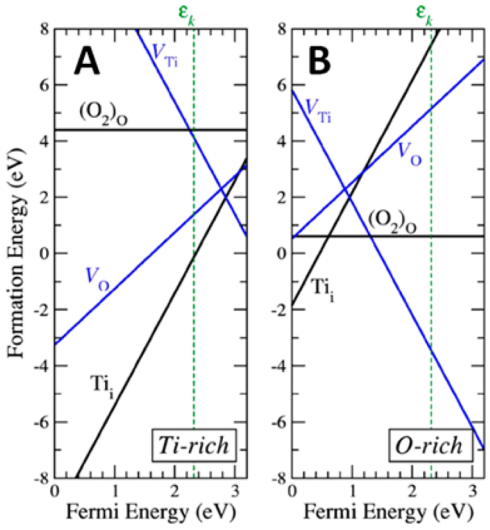


**Figure 32.** DFT-calculated defect formation energies in bulk anatase as a function of the $E_F$ under the Ti-rich (A) and O-rich (B) growth conditions, respectively. The slope of the line indicates the charge state of the defect. The Fermi energy is referenced to the top of the valence band. Vertical dotted line is the calculated band gap at the special *k* point.[316] (Reprinted with permission from ref 316. Copyright 2006 The American Physical Society.)

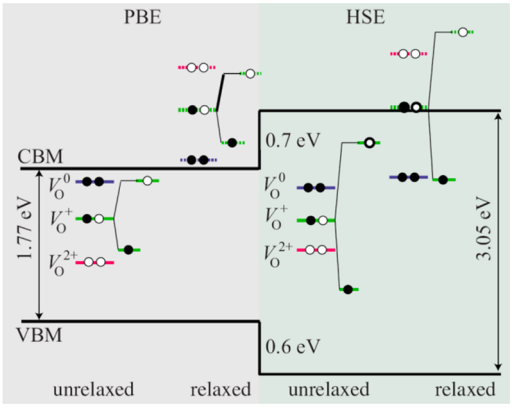


**Figure 33.** Calculated position of the single-particle $a_1$ state of the $V_O$ in $TiO_2$. PBE and HSE band structures were aligned as described in the text. Results for various charge states and for both unrelaxed and relaxed vacancies are shown. For $V_O^+$, the position of the $a_1$ state in both spin-up and spin-down channels is also indicated. Positions of states above the CBM were estimated based on projected densities-of-states on the three nearest-neighbor Ti atoms and are represented by dashed lines.[321] (Reprinted with permission from ref 321. Copyright 2010 The American Physical Society.)

cally break into isolated interstitials and vacancies.[316] $Ti_i$, $O_i$, $V_{Ti}$, and $V_O$ produced no defect levels to the band gap.[316]

Despite the detailed DFT descriptions given on the electronic properties of point defects in $TiO_2$ there were arguments that such approaches based on pure exchange−correlation functionals cannot satisfactorily reproduce the experimental findings.[319,320] Di Valentin et al. pointed out that limited by the insufficient cancelation of the self-interaction energy pure DFT functionals might fail in describing the localized states, particularly of excess holes and electrons in wide-band-gap semiconductors and insulators such as $V_O$ centers in $TiO_2$.[319,320] They suggested that inclusion of a Hartree−Fock (HF) exchange or Hubbard term (GGA+U) enhanced the Ti $3d^1$ defect state description and induced the polaronic distortion.[319,320] With the help of spin-polarized hybrid DFT calculations they investigated the $Ti_i$ atom's charge and spin state in reduced bulk anatase and rutile $TiO_2$.[320] A $Ti_i$ atom in an interstitial cavity instantly turned into a $Ti^{3+}$ ion, donating three electrons to the lattice Ti ions and keeping one on its 3d shell. Both interstitial and lattice $Ti^{3+}$ ions induced new states near 1.0−1.5 eV below the CBM in the band gap.[320] These states were spread in an interval of 0.7−0.8 eV as they were exposed to different adjacent environments.[320] Janotti et al. investigated $V_O$ in rutile with the hybrid functionals.[321] $V_O$ was a shallow donor in the band gap, and the energy of the +2 charge state ($V_O^{2+}$) was lower than the +1 charge ($V_O^{1+}$) and neutral states (Figure 33).[321] The low formation energy of $V_O^{2+}$ explained the n-type conductivity of $TiO_2$ single crystals heated under O-poor conditions.[321]

## 8. SUMMARY

Self-structural modification is indeed not new to the extensive research so far on $TiO_2$. Rather than concerning the properties from alien atoms or substances it describes the structural deviation of different phases of $TiO_2$. In fact, structural deviation may originate from porous, amorphous, mixed-phase, disordered, or low-dimensional $TiO_2$, where the chemical bondings deviate from the specific bulk styles more or less and bring the adjustments to its electronic properties. Any structural deviation from the bulk value would expect to bring up corresponding electronic, optical, and photocatalytic property changes, as these properties depend largely on the couplings of the atomic orbitals (O 2p and Ti 3d for $TiO_2$) which are a function of the structural parameters.

Surface effects are observed to cause dramatic electronic and optical property changes due to the unsaturated atoms and the reconstructed morphology. Lattice strain, which causes the lattice parameter changes, apparently brings up additional electronic structural changes. Reducing the size of $TiO_2$ to the nanometer scale, i.e., below its Bohr radius values, largely magnifies these surface and lattice-strain effects, with an increase of the ratio of surface atoms and the lattice deviation in the $TiO_2$ nanomaterials compared to their bulk counterparts.

Coupling one phase with another in the mixed $TiO_2$ composite has proven to be efficient in improving its photocatalytic performance from the synergistic effects. The synergistic effects may include better charge separation, long-wavelength antenna, and catalytic "hot spots" at the interface, which is experimentally and theoretically suggested to be involved with structural disorders. The direction of the photogenerated charge flow across the interface in the heterogeneous composite depends on the relative positions of the electronic structures (CBM and VBM) and their interfacial atomic structures. Both experimental measurements and theoretical simulations show the interfacial structures feature with disordered phases. Further investigations on the atomic bonding information are apparently needed to understand better the synergistic effects in composite nanomaterials, such as anatase/rutile, brookite/anatase, and brookite/rutile mixtures.

Disordered and amorphous phases are apparently still among the most challenging tasks to tackle both experimentally and theoretically, partially due to the lack of control of the basic structural parameters of these phases. Thus, the progress in this field is relatively not prominent.


dx.doi.org/10.1021/cr400624r | *Chem. Rev.* 2014, 114, 9890−9918

$$TiO_2 + xH_2 \xrightarrow{\Delta} TiO_2,\ TiO_{2-x},\ TiO_{2-x}H_{2x}...? \quad (8)$$

Although the chemical reaction in the hydrogen treatment of $TiO_2$ nanocrystals seems to be simple and straightforward, the reaction mechanism, the resultant products, and their properties are still not conclusive (eq 8). Contradictory results have been constantly reported on the physical properties, chemical properties, and photocatalytic performance of hydrogenated $TiO_2$ nanocrystals. Observations of structural disorder or not, appearance of $Ti^{3+}$, Ti−H, and oxygen vacancy or not, increase or decrease of the signal of Ti−OH, and shift of the VB band edge or not are all under debate, besides the different interpretations from the theoretical calculations. One of the reasons could be inherent in the complicated nature of this reaction itself. Another reason could be experimental, as samples from different groups are normally prepared under different conditions. These conditions may directly change the reaction pathways and thus the final properties of the hydrogenated $TiO_2$ nanomaterials. Nevertheless, hydrogenated $TiO_2$ nanomaterials have been shown with enhanced performance in many applications, including photocatalysis, lithium-ion battery, supercapacitor, fuel cell, field emission, and microwave absorption. Further investigation may reveal more information on the underlying reaction mechanisms as well as the physiochemical properties and thus open new applications for hydrogenated $TiO_2$ nanomaterials.

The debate on the fundamental properties may seek help from traditional defect chemistry and physics, where the stoichiometric chemistry of $TiO_2$ may no longer hold and large structural deviations exist. These may involve the broad variations of bond angle and bond length; it would be necessary to consider the overall changes of the chemical environment rather than to focus locally on the defects, such as $Ti^{3+}$ or $V_O$.

In brief, self-structural modification has been proven especially useful for enhancing its advanced functionalities for $TiO_2$ nanomaterials, such as in photocatalytic application for harvesting solar energy. The insight obtained thus may be transferred to other oxide nanomaterials in various applications.

## AUTHOR INFORMATION

### Corresponding Authors

*E-mail: liulei@ciomp.ac.cn.
*E-mail: chenxiaobo@umkc.edu.

### Notes

The authors declare no competing financial interest.

### Biographies

Lei Liu obtained his Ph.D. degree in Physics from National University of Singapore and B.Sc. and M.Sc. degrees in Condensed Matter Physics at Jilin University. With the support from the "100 Talents Program of Chinese Academy of Sciences", in 2011 he joined State Key Laboratory of Luminescence and Applications at Changchun Institute of Optics, Fine Mechanics and Physics of Chinese Academy of Sciences. He is a professor of the institute, and his current research interests are mainly involved with electronic and optical properties of semiconductors.

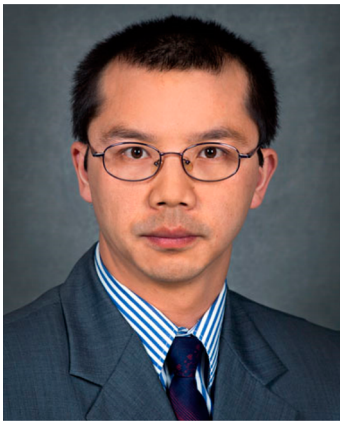

Xiaobo Chen obtained his Ph.D. degree in Chemistry from Case Western Reserve University in the United States in 2005 and then worked at the University of California—Berkeley and Lawrence Berkeley National Laboratory. He joined the University of Missouri—Kansas City (UMKC) in the fall of 2011. He has published around 50 articles with over 12 000 citations. He is currently an assistant professor of Chemistry at UMKC, and his research interests include nanomaterials, adsorbents, photocatalysis, and batteries for energy and environmental applications.

## ACKNOWLEDGMENTS

X.C. is thankful for support from the College of Arts and Sciences, the University of Missouri—Kansas City, and the University of Missouri Research Board. L.L. acknowledges the support of the 100 Talents Program of the Chinese Academy of Sciences.

## REFERENCES

(1) von Bichowsky, F. *Ind. Eng. Chem.* **1929**, *21*, 1061.
(2) Braun, J. H.; Baidins, A.; Marganski, R. E. *Prog. Org. Coat.* **1992**, *20*, 105.
(3) Phillips, L. G.; Barbano, D. M. *J. Dairy Sci.* **1997**, *80*, 2726.
(4) Salvador, A.; Pascual-Marti, M. C.; Adell, J. R.; Requeni, A.; March, J. G. *J. Pharm. Biomed. Anal.* **2000**, *22*, 301.
(5) Zallen, R.; Moret, M. P. *Solid State Commun.* **2006**, *137*, 154.
(6) Braun, J. H. *J. Coat. Technol.* **1997**, *69*, 59.
(7) Fujishima, A.; Honda, K. *Nature* **1972**, *238*, 37.
(8) Mills, A.; LeHunte, S. *J. Photochem. Photobiol. A: Chem.* **1997**, *108*, 1.
(9) Chen, X.; Mao, S. S. *Chem. Rev.* **2007**, *107*, 2891.
(10) Chen, X. *Chin. J. Catal.* **2009**, *30*, 839.
(11) Borgarello, E.; Kiwi, J.; Pelizzetti, E.; Visca, M.; Gratzel, M. *Nature* **1981**, *289*, 158.
(12) Duonghong, D.; Borgarello, E.; Gratzel, M. *J. Am. Chem. Soc.* **1981**, *103*, 4685.
(13) Chen, X.; Shen, S.; Guo, L.; Mao, S. S. *Chem. Rev.* **2010**, *110*, 6503.
(14) Chen, X.; Li, C.; Graetzel, M.; Kostecki, R.; Mao, S. S. *Chem. Soc. Rev.* **2012**, *41*, 7909.

(15) Walter, M. G.; Warren, E. L.; McKone, J. R.; Boettcher, S. W.; Mi, Q.; et al. *Chem. Rev.* **2010**, *110*, 6446.
(16) Shimura, K.; Yoshida, H. *Energy Environ. Sci.* **2011**, *4*, 2467.
(17) Murdoch, M.; Waterhouse, G. I. N.; Nadeem, M. A.; Metson, J. B.; et al. *Nat. Chem.* **2011**, *3*, 489.
(18) Kraeutler, B.; Bard, A. J. *J. Am. Chem. Soc.* **1978**, *100*, 5985.
(19) Reiche, H.; Bard, A. J. *J. Am. Chem. Soc.* **1979**, *101*, 3127.
(20) Hoffmann, M. R.; Martin, S. T.; Choi, W. Y.; Bahnemann, D. W. *Chem. Rev.* **1995**, *95*, 69.
(21) Fujishima, A.; Rao, T. N.; Tryk, D. A. *J. Photochem. Photobiol. C: Photochem. Rev.* **2000**, *1*, 1.
(22) Tryk, D. A.; Fujishima, A.; Honda, K. *Electrochim. Acta* **2000**, *45*, 2363.
(23) Linsebigler, A. L.; Lu, G. Q.; Yates, J. T. *Chem. Rev.* **1995**, *95*, 735.
(24) Wold, A. *Chem. Mater.* **1993**, *5*, 280.
(25) Han, F.; Kambala, V. S. R.; Srinivasan, M.; Rajarathnam, D.; Naidu, R. *Appl. Catal., A* **2009**, *359*, 25.
(26) Inoue, T.; Fujishima, A.; Konishi, S.; Honda, K. *Nature* **1979**, *277*, 637.
(27) Anpo, M.; Chiba, K. *J. Mol. Catal.* **1992**, *74*, 207.
(28) Mizuno, T.; Adachi, K.; Ohta, K.; Saji, A. *J. Photochem. Photobiol. A: Chem.* **1996**, *98*, 87.
(29) Kaneco, S.; Shimizu, Y.; Ohta, K.; Mizuno, T. *J. Photochem. Photobiol. A: Chem.* **1998**, *115*, 223.
(30) Tan, S. S.; Zou, L.; Hu, E. *Int. J. Green Energy* **2006**, *3*, 283.
(31) Tan, S. S.; Zou, L.; Hu, E. *Catal. Today* **2006**, *115*, 269.
(32) Habisreutinger, S. N.; Schmidt-Mende, L.; Stolarczyk, J. K. *Angew. Chem., Int. Ed.* **2013**, *52*, 7372.
(33) Appel, A. M.; Bercaw, J. E.; Bocarsly, A. B.; Dobbek, H.; et al. *Chem. Rev.* **2013**, *113*, 6621.
(34) Liu, G.; Hoivik, N.; Wang, K.; Jakobsen, H. *Sol. Energy Mater. Sol. Cells* **2012**, *105*, 53.
(35) Izumi, Y. *Coord. Chem. Rev.* **2013**, *257*, 171.
(36) Dhakshinamoorthy, A.; Navalon, S.; Corma, A.; Garcia, H. *Energy Environ. Sci.* **2012**, *5*, 9217.
(37) Li, X.; Liu, H.; Luo, D.; Li, J.; et al. *Chem. Eng. J.* **2012**, *180*, 151.
(38) Yang, C.-C.; Yu, Y.-H.; van der Linden, B.; Wu, J. C. S.; Mul, G. *J. Am. Chem. Soc.* **2010**, *132*, 8398.
(39) Richardson, R. D.; Holland, E. J.; Carpenter, B. K. *Nat. Chem.* **2011**, *3*, 301.
(40) Wang, P.-Q.; Bai, Y.; Liu, J.-Y.; Fan, Z.; Hu, Y.-Q. *Catal. Commun.* **2012**, *29*, 185.
(41) Green, I. X.; Tang, W. J.; Neurock, M.; Yates, J. T. *Science* **2011**, *333*, 736.
(42) Gratzel, M. *Nature* **2001**, *414*, 338.
(43) Hagfeldt, A.; Gratzel, M. *Chem. Rev.* **1995**, *95*, 49.
(44) Hains, A. W.; Liang, Z.; Woodhouse, M. A.; Gregg, B. A. *Chem. Rev.* **2010**, *110*, 6689.
(45) Graetzel, M. *Acc. Chem. Res.* **2009**, *42*, 1788.
(46) Yang, Z.; Choi, D.; Kerisit, S.; Rosso, K. M.; Wang, D.; et al. *J. Power Sources* **2009**, *192*, 588.
(47) Hu, Y. S.; Kienle, L.; Guo, Y. G.; Maier, J. *Adv. Mater.* **2006**, *18*, 1421.
(48) Baudrin, E.; Cassaignon, S.; Koesch, M.; Jolivet, J. P.; Dupont, L.; et al. *Electrochem. Commun.* **2007**, *9*, 337.
(49) Brutti, S.; Gentili, V.; Menard, H.; Scrosati, B.; Bruce, P. G. *Adv. Energy Mater.* **2012**, *2*, 322.
(50) Lindstrom, H.; Sodergren, S.; Solbrand, A.; Rensmo, H.; Hjelm, J.; et al. *J. Phys. Chem. B* **1997**, *101*, 7717.
(51) Xia, T.; Zhang, W.; Murowchick, J.; Liu, G.; Chen, X. *Adv. Energy Mater.* **2013**, *3*, 1516.
(52) Xia, T.; Zhang, W.; Li, W.; Oyler, N. A.; Liu, G.; Chen, X. *Nano Energy* **2013**, *2*, 826.
(53) Benkstein, K. D.; Semancik, S. *Sens. Actuators B: Chem.* **2006**, *113*, 445.
(54) Ferroni, M.; Carotta, M. C.; Guidi, V.; Martinelli, G.; Ronconi, F.; et al. *Sens. Actuators B: Chem.* **2000**, *68*, 140.
(55) Trinchi, A.; Li, Y. X.; Wlodarski, W.; Kaciulis, S.; Pandolfi, L.; et al. *Sens. Actuators B: Chem.* **2003**, *95*, 145.
(56) Jun, Y. K.; Kim, H. S.; Lee, J. H.; Hong, S. H. *Sens. Actuators B: Chem.* **2005**, *107*, 264.
(57) Carney, C. M.; Yoo, S.; Akbar, S. A. *Sens. Actuators B: Chem.* **2005**, *108*, 29.
(58) Markowska-Szczupak, A.; Ulfig, K.; Morawski, A. W. *Catal. Today* **2011**, *169*, 249.
(59) Zhang, Y.; Harris, C. X.; Wallenmeyer, P.; Murowchick, J.; Chen, X. *J. Phys. Chem. C* **2013**, *117*, 24015.
(60) Choi, W. Y.; Termin, A.; Hoffmann, M. R. *J. Phys. Chem.* **1994**, *98*, 13669.
(61) Choi, W. Y.; Termin, A.; Hoffmann, M. R. *Angew. Chem., Int. Ed. Engl.* **1994**, *33*, 1091.
(62) Anpo, M.; Kishiguchi, S.; Ichihashi, Y.; Takeuchi, M.; Yamashita, H.; et al. *Res. Chem. Intermed.* **2001**, *27*, 459.
(63) Bryan, J. D.; Heald, S. M.; Chambers, S. A.; Gamelin, D. R. *J. Am. Chem. Soc.* **2004**, *126*, 11640.
(64) Asahi, R.; Morikawa, T.; Ohwaki, T.; Aoki, K.; Taga, Y. *Science* **2001**, *293*, 269.
(65) Khan, S. U. M.; Al-Shahry, M.; Ingler, W. B. *Science* **2002**, *297*, 2243.
(66) Burda, C.; Lou, Y. B.; Chen, X.; Samia, A. C. S.; Stout, J.; et al. *Nano Lett.* **2003**, *3*, 1049.
(67) Chen, X.; Burda, C. *J. Phys. Chem. B* **2004**, *108*, 15446.
(68) Chen, X.; Lou, Y. B.; Samia, A. C. S.; Burda, C.; Gole, J. L. *Adv. Funct. Mater.* **2005**, *15*, 41.
(69) Chen, X.; Burda, C. *J. Am. Chem. Soc.* **2008**, *130*, 5018.
(70) Anpo, M.; Takeuchi, M. *J. Catal.* **2003**, *216*, 505.
(71) Kubacka, A.; Fernandez-Garcia, M.; Colon, G. *Chem. Rev.* **2012**, *112*, 1555.
(72) Kumar, S. G.; Devi, L. G. *J. Phys. Chem. A* **2011**, *115*, 13211.
(73) Zhou, M.; Yu, J.; Liu, S.; Zhai, P.; Jiang, L. *J. Hazard. Mater.* **2008**, *154*, 1141.
(74) Hattori, A.; Tokihisa, Y.; Tada, H.; Tohge, N.; Ito, S.; et al. *J. Sol-Gel Sci. Technol.* **2001**, *22*, 53.
(75) Wu, L.; Yu, J. C.; Fu, X. Z. *J. Mol. Catal. A: Chem.* **2006**, *244*, 25.
(76) Jang, J. S.; Li, W.; Oh, S. H.; Lee, J. S. *Chem. Phys. Lett.* **2006**, *425*, 278.
(77) Nazeeruddin, M. K.; Kay, A.; Rodicio, I.; Humphrybaker, R.; Muller, E.; et al. *J. Am. Chem. Soc.* **1993**, *115*, 6382.
(78) Nazeeruddin, M. K.; Pechy, P.; Gratzel, M. *Chem. Commun.* **1997**, 1705.
(79) Hashimoto, K.; Irie, H.; Fujishima, A. *Jpn. J. Appl. Phys., Part 1* **2005**, *44*, 8269.
(80) Liu, L.; Yu, P. Y.; Chen, X.; Mao, S. S.; Shen, D. Z. *Phys. Rev. Lett.* **2013**, *111*, 5505.
(81) Park, J. H.; Kim, S.; Bard, A. J. *Nano Lett.* **2006**, *6*, 24.
(82) Umebayashi, T.; Yamaki, T.; Itoh, H.; Asai, K. *Appl. Phys. Lett.* **2002**, *81*, 454.
(83) He, J.; Liu, Q.; Sun, Z.; Yan, W.; Zhang, G.; et al. *J. Phys. Chem. C* **2010**, *114*, 6035.
(84) Irie, H.; Watanabe, Y.; Hashimoto, K. *Chem. Lett.* **2003**, *32*, 772.
(85) Gai, Y.; Li, J.; Li, S.-S.; Xia, J.-B.; Wei, S.-H. *Phys. Rev. Lett.* **2009**, *102*, 036402.
(86) Dong, P.; Liu, B.; Wang, Y.; Pei, H.; Yin, S. *J. Mater. Res.* **2010**, *25*, 2392.
(87) Zhang, J.; Pan, C.; Fang, P.; Wei, J.; Xiong, R. *ACS Appl. Mater. Interfaces* **2010**, *2*, 1173.
(88) Liu, H.; Lu, Z.; Yue, L.; Liu, J.; Gan, Z.; et al. *Appl. Surf. Sci.* **2011**, *257*, 9355.
(89) Liu, Y.; Shu, W.; Chen, K.; Peng, Z.; Chen, W. *ACS Catal.* **2012**, *2*, 2557.
(90) Yang, F.; Yang, H.; Tian, B.; Zhang, J.; He, D. *Res. Chem. Intermed.* **2013**, *39*, 1685.
(91) Zhang, J.; Xi, J.; Ji, Z. *J. Mater. Chem.* **2012**, *22*, 17700.
(92) Li, X.; Chen, Z.; Shi, Y.; Liu, Y. *Powder Technol.* **2011**, *207*, 165.
(93) Li, K.; Wang, H.; Pan, C.; Wei, J.; Xiong, R.; et al. *Int. J. Photoenergy* **2012**, *2012*, 398508.

(94) Kim, T.-H.; Rodriguez-Gonzalez, V.; Gyawali, G.; Cho, S.-H.; Sekino, T.; et al. *Catal. Today* **2013**, *212*, 75.
(95) Hoang, S.; Guo, S.; Mullins, C. B. *J. Phys. Chem. C* **2012**, *116*, 23283.
(96) Zhang, Y.; Li, C.; Pan, C. *J. Am. Ceram. Soc.* **2012**, *95*, 2951.
(97) Xiao, Q.; Gao, L. *J. Alloys Compd.* **2013**, *551*, 286.
(98) Nakamura, I.; Negishi, N.; Kutsuna, S.; Ihara, T.; Sugihara, S.; et al. *J. Mol. Catal. A: Chem.* **2000**, *161*, 205.
(99) Pan, X.; Yang, M.-Q.; Fu, X.; Zhang, N.; Xu, Y.-J. *Nanoscale* **2013**, *5*, 3601.
(100) Takeuchi, K.; Nakamura, I.; Matsumoto, O.; Sugihara, S.; Ando, M.; et al. *Chem. Lett.* **2000**, 1354.
(101) Ihara, T.; Miyoshi, M.; Ando, M.; Sugihara, S.; Iriyama, Y. *J. Mater. Sci.* **2001**, *36*, 4201.
(102) Chen, X.; Liu, L.; Yu, P. Y.; Mao, S. S. *Science* **2011**, *331*, 746.
(103) Tachibana, Y.; Vayssieres, L.; Durrant, J. R. *Nat. Photonics* **2012**, *6*, 511.
(104) Diebold, U. *Nat. Chem.* **2011**, *3*, 271.
(105) Zhu, Q.; Qian, J.; Pan, H.; Tu, L.; Zhou, X. *Nanotechnology* **2011**, *22*, 395703.
(106) Kang, T.-S.; Smith, A. P.; Taylor, B. E.; Durstock, M. F. *Nano Lett.* **2009**, *9*, 601.
(107) Sauvage, F.; Di Fonzo, F.; Bassi, A. L.; Casari, C. S.; Russo, V.; et al. *Nano Lett.* **2010**, *10*, 2562.
(108) Kuang, D.; Brillet, J.; Chen, P.; Takata, M.; Uchida, S.; et al. *ACS Nano* **2008**, *2*, 1113.
(109) Jiao, W.; Wang, L.; Liu, G.; Lu, G. Q.; Cheng, H.-M. *ACS Catal.* **2012**, *2*, 1854.
(110) Zhao, X.; Jin, W.; Cai, J.; Ye, J.; et al. *Adv. Funct. Mater.* **2011**, *21*, 3554.
(111) Yang, W.-G.; Wan, F.-R.; Chen, Q.-W.; Li, J.-J.; Xu, D.-S. *J. Mater. Chem.* **2010**, *20*, 2870.
(112) Chen, D.; Huang, F.; Cheng, Y.-B.; Caruso, R. A. *Adv. Mater.* **2009**, *21*, 2206.
(113) Robben, L.; Ismail, A. A.; Lohmeier, S. J.; Feldhoff, A.; et al. *Chem. Mater.* **2012**, *24*, 1268.
(114) Tetreault, N.; Horvath, E.; Moehl, T.; Brillet, J.; Smajda, R.; et al. *ACS Nano* **2010**, *4*, 7644.
(115) Sauvage, F.; Chen, D.; Comte, P.; Huang, F.; Heiniger, L.-P.; et al. *ACS Nano* **2010**, *4*, 4420.
(116) Zheng, W.; Liu, X.; Yan, Z.; Zhu, L. *ACS Nano* **2009**, *3*, 115.
(117) Kho, Y. K.; Iwase, A.; Teoh, W. Y.; Maedler, L.; Kudo, A.; et al. *J. Phys. Chem. C* **2010**, *114*, 2821.
(118) Ohtani, B.; Prieto-Mahaney, O. O.; Li, D.; Abe, R. *J. Photochem. Photobiol. A: Chem.* **2010**, *216*, 179.
(119) Deak, P.; Aradi, B.; Frauenheim, T. *J. Phys. Chem. C* **2011**, *115*, 3443.
(120) Kandiel, T. A.; Feldhoff, A.; Robben, L.; Dillert, R.; Bahnemann, D. W. *Chem. Mater.* **2010**, *22*, 2050.
(121) Knorr, F. J.; Mercado, C. C.; McHale, J. L. *J. Phys. Chem. C* **2008**, *112*, 12786.
(122) Li, G.; Gray, K. A. *Chem. Mater.* **2007**, *19*, 1143.
(123) Alivisatos, A. P. *J. Phys. Chem.* **1996**, *100*, 13226.
(124) Burda, C.; Chen, X.; Narayanan, R.; El-Sayed, M. A. *Chem. Rev.* **2005**, *105*, 1025.
(125) Macwan, D. P.; Dave, P. N.; Chaturvedi, S. *J. Mater. Sci.* **2011**, *46*, 3669.
(126) Pfaff, G.; Reynders, P. *Chem. Rev.* **1999**, *99*, 1963.
(127) Diebold, U. *Surf. Sci. Rep.* **2003**, *48*, 53.
(128) Henderson, M. A. *Surf. Sci. Rep.* **2011**, *66*, 185.
(129) Grant, F. A. *Rev. Mod. Phys.* **1959**, *31*, 646.
(130) Mo, S. D.; Ching, W. Y. *Phys. Rev. B* **1995**, *51*, 13023.
(131) Hanaor, D. A. H.; Sorrell, C. C. *J. Mater. Sci.* **2011**, *46*, 855.
(132) Marchand, R.; Brohan, L.; Tournoux, M. *Mater. Res. Bull.* **1980**, *15*, 1129.
(133) Banfield, J. F.; Veblen, D. R.; Smith, D. J. *Am. Mineral.* **1991**, *76*, 343.
(134) Chen, S.; Zhu, Y.; Li, W.; Liu, W.; Li, L.; et al. *Chin. J. Catal.* **2010**, *31*, 605.
(135) Muscat, J.; Swamy, V.; Harrison, N. M. *Phys. Rev. B* **2002**, *65*, 224112.
(136) Cromer, D. T.; Herrington, K. *J. Am. Chem. Soc.* **1955**, *77*, 4708.
(137) Baur, W. H. *Acta Crystallogr.* **1961**, *14*, 214.
(138) Samsonov, G. V. *The Oxide Handbook*, 2nd ed.; IFI/Plenum Press: New York, 1982.
(139) Gribb, A. A.; Banfield, J. F. *Am. Mineral.* **1997**, *82*, 717.
(140) Landmann, M.; Rauls, E.; Schmidt, W. G. *J. Phys.: Condens. Matter* **2012**, *24*, 195503.
(141) Ranade, M. R.; Navrotsky, A.; Zhang, H. Z.; Banfield, J. F.; Elder, S. H.; et al. *Proc. Natl. Acad. Sci. U.S.A.* **2002**, *99*, 6476.
(142) Wang, J. W.; Mishra, A. K.; Zhao, Q.; Huang, L. *J. Phys. D* **2013**, *46*, 255303.
(143) Zhang, H. Z.; Banfield, J. F. *J. Phys. Chem. B* **2000**, *104*, 3481.
(144) Gouma, P. I.; Mills, M. J. *J. Am. Ceram. Soc.* **2001**, *84*, 619.
(145) Deskins, N. A.; Kerisit, S.; Rosso, K. M.; Dupuis, M. *J. Phys. Chem. C* **2007**, *111*, 9290.
(146) Farfan-Arribas, E.; Madix, R. J. *J. Phys. Chem. B* **2003**, *107*, 3225.
(147) Martra, G. *Appl. Catal., A* **2000**, *200*, 275.
(148) Wang, R.; Hashimoto, K.; Fujishima, A.; Chikuni, M.; Kojima, E.; et al. *Nature* **1997**, *388*, 431.
(149) Charlton, G.; Howes, P. B.; Nicklin, C. L.; Steadman, P.; Taylor, J. S. G.; et al. *Phys. Rev. Lett.* **1997**, *78*, 495.
(150) Hird, B.; Armstrong, R. A. *Surf. Sci.* **1999**, *420*, L131.
(151) Hird, B.; Armstrong, R. A. *Surf. Sci.* **1997**, *385*, L1023.
(152) Henderson, M. A. *Langmuir* **1996**, *12*, 5093.
(153) Henderson, M. A. *Surf. Sci.* **1999**, *419*, 174.
(154) Henrich, V. E.; Dresselhaus, G.; Zeiger, H. J. *Phys. Rev. Lett.* **1976**, *36*, 1335.
(155) Kurtz, R. L.; Stockbauer, R.; Madey, T. E.; Roman, E.; Desegovia, J. L. *Surf. Sci.* **1989**, *218*, 178.
(156) Epling, W. S.; Peden, C. H. F.; Henderson, M. A.; Diebold, U. *Surf. Sci.* **1998**, *412*−*13*, 333.
(157) Zhang, Z. M.; Jeng, S. P.; Henrich, V. E. *Phys. Rev. B* **1991**, *43*, 12004.
(158) Yim, C. M.; Pang, C. L.; Thornton, G. *Phys. Rev. Lett.* **2010**, *104*, 036806.
(159) Papageorgiou, A. C.; Beglitis, N. S.; Pang, C. L.; Teobaldi, G.; et al. *Proc. Natl. Acad. Sci. U.S.A.* **2010**, *107*, 2391.
(160) Ariga, H.; Taniike, T.; Morikawa, H.; Tada, M.; Min, B. K.; et al. *J. Am. Chem. Soc.* **2009**, *131*, 14670.
(161) Tao, J.; Luttrell, T.; Batzill, M. *Nat. Chem.* **2011**, *3*, 296.
(162) Shibata, T.; Irie, H.; Hashimoto, K. *J. Phys. Chem. B* **2003**, *107*, 10696.
(163) Tavares, C. J.; Marques, S. M.; Rebouta, L.; Lanceros-Mendez, S.; Sencadas, V.; et al. *J. Thin Solid Films* **2008**, *517*, 1161.
(164) Kamei, M.; Miyagi, T.; Ishigaki, T. *Chem. Phys. Lett.* **2005**, *407*, 209.
(165) Grey, I. E.; Wilson, N. C. *J. Solid State Chem.* **2007**, *180*, 670.
(166) Swamy, V.; Kuznetsov, A. Y.; Dubrovinsky, L. S.; Kurnosov, A.; Prakapenka, V. B. *Phys. Rev. Lett.* **2009**, *103*, 075505.
(167) Arlt, T.; Bermejo, M.; Blanco, M. A.; Gerward, L.; Jiang, J. Z.; et al. *Phys. Rev. B* **2000**, *61*, 14414.
(168) Swamy, V.; Dubrovinsky, L. S. *J. Phys. Chem. Solids* **2001**, *62*, 673.
(169) Yin, W.-J.; Chen, S.; Yang, J.-H.; Gong, X.-G.; Yan, Y.; et al. *Appl. Phys. Lett.* **2010**, *96*, 221901.
(170) Wagner, J. M.; Bechstedt, F. *Phys. Rev. B* **2002**, *66*, 115202.
(171) Vandewalle, C. G. *Phys. Rev. B* **1989**, *39*, 1871.
(172) Thulin, L.; Guerra, J. *Phys. Rev. B* **2008**, *77*, 195112.
(173) Yan, J.; Wu, G.; Guan, N.; Li, L.; et al. *Phys. Chem. Chem. Phys.* **2013**, *15*, 10978.
(174) Anpo, M.; Shima, T.; Kodama, S.; Kubokawa, Y. *J. Phys. Chem.* **1987**, *91*, 4305.
(175) Kavan, L.; Stoto, T.; Gratzel, M.; Fitzmaurice, D.; Shklover, V. *J. Phys. Chem.* **1993**, *97*, 9493.

(176) Kormann, C.; Bahnemann, D. W.; Hoffmann, M. R. *J. Phys. Chem.* **1988**, *92*, 5196.
(177) Brus, L. *J. Phys. Chem.* **1986**, *90*, 2555.
(178) Nosaka, Y. *J. Phys. Chem.* **1991**, *95*, 5054.
(179) Henglein, A. *Chem. Rev.* **1989**, *89*, 1861.
(180) Nakajima, R.; Tsuruta, M.; Higuchi, M.; Yamamoto, K. *J. Am. Chem. Soc.* **2004**, *126*, 1630.
(181) Satoh, N.; Nakashima, T.; Kamikura, K.; Yamamoto, K. *Nat. Nanotechnol.* **2008**, *3*, 106.
(182) Li, Y.; White, T. J.; Lim, S. H. *J. Solid State Chem.* **2004**, *177*, 1372.
(183) Reddy, K. M.; Reddy, C. V. G.; Manorama, S. V. *J. Solid State Chem.* **2001**, *158*, 180.
(184) Serpone, N.; Lawless, D.; Khairutdinov, R. *J. Phys. Chem.* **1995**, *99*, 16646.
(185) Serpone, N.; Lawless, D.; Khairutdinov, R.; Pelizzetti, E. *J. Phys. Chem.* **1995**, *99*, 16655.
(186) Monticone, S.; Tufeu, R.; Kanaev, A. V.; Scolan, E.; Sanchez, C. *Appl. Surf. Sci.* **2000**, *162*, 565.
(187) Balducci, G.; Gigli, G.; Guido, M. *J. Chem. Phys.* **1985**, *83*, 1909.
(188) Balducci, G.; Gigli, G.; Guido, M. *J. Chem. Phys.* **1985**, *83*, 1913.
(189) Wu, H. B.; Wang, L. S. *J. Chem. Phys.* **1997**, *107*, 8221.
(190) Zhai, H. J.; Wang, L. S. *J. Am. Chem. Soc.* **2007**, *129*, 3022.
(191) Woodley, S. M.; Hamad, S.; Mejias, J. A.; Catlow, C. R. A. *J. Mater. Chem.* **2006**, *16*, 1927.
(192) Qu, Z. W.; Kroes, G. J. *J. Phys. Chem. B* **2006**, *110*, 8998.
(193) Shevlin, S. A.; Woodley, S. M. *J. Phys. Chem. C* **2010**, *114*, 17333.
(194) Chiodo, L.; Salazar, M.; Romero, A. H.; Laricchia, S.; Della Sala, F.; et al. *J. Chem. Phys.* **2011**, 135.
(195) Guisbiers, G.; Van Overschelde, O.; Wautelet, M. *Appl. Phys. Lett.* **2008**, *92*, 103121.
(196) Wautelet, M. *Phys. Lett. A* **1998**, *246*, 341.
(197) Guisbiers, G.; Pereira, S. *Nanotechnology* **2007**, *18*, 435710.
(198) Keller, S. P. *Handbook on Semiconductors: Materials, Properties and Preparation*; North-Holland, Amsterdam, 1980; Vol. *3*.
(199) Li, M.; Li, J. C. *Mater. Lett.* **2006**, *60*, 2526.
(200) Yang, C. C.; Jiang, Q. *Mater. Sci. Eng., B* **2006**, *131*, 191.
(201) Swamy, V.; Menzies, D.; Muddle, B. C.; Kuznetsov, A.; Dubrovinsky, L. S.; et al. *Appl. Phys. Lett.* **2006**, 88.
(202) Bokhimi; Morales, A.; Novaro, O.; Lopez, T.; Sanchez, E.; Gomez, R. *J. Mater. Res.* **1995**, *10*, 2788.
(203) Grey, I.; Madsen, I.; Bordet, P.; Wilson, N.; Li, C. *Advances in Ecomaterials*; Stallion Press: Singapore, 2005, Vol. *1*.
(204) Su, W. G.; Zhang, J.; Feng, Z. C.; Chen, T.; Ying, P. L.; et al. *J. Phys. Chem. C* **2008**, *112*, 7710.
(205) Zhang, J.; Li, M. J.; Feng, Z. C.; Chen, J.; Li, C. *J. Phys. Chem. B* **2006**, *110*, 927.
(206) Lee, G. H.; Zuo, H. M. *J. Am. Ceram. Soc.* **2004**, *87*, 473.
(207) Penn, R. L.; Banfield, J. F. *Am. Mineral.* **1999**, *84*, 871.
(208) Zhang, J.; Xu, Q.; Li, M. J.; Feng, Z. C.; Li, C. *J. Phys. Chem. C* **2009**, *113*, 1698.
(209) Satoh, N.; Nakashima, T.; Yamamoto, K. *Sci. Rep.* **2013**, *3*, 1959.
(210) Lin, H.; Huang, C. P.; Li, W.; Ni, C.; Shah, S. I.; et al. *Appl. Catal., B* **2006**, *68*, 1.
(211) Hurum, D. C.; Agrios, A. G.; Gray, K. A.; Rajh, T.; Thurnauer, M. C. *J. Phys. Chem. B* **2003**, *107*, 4545.
(212) Ohno, T.; Tokieda, K.; Higashida, S.; Matsumura, M. *Appl. Catal., A* **2003**, *244*, 383.
(213) Bacsa, R. R.; Kiwi, J. *Appl. Catal., B* **1998**, *16*, 19.
(214) Zhang, X. R.; Lin, Y. H.; He, D. Q.; Zhang, J. F.; Fan, Z. Y.; et al. *Chem. Phys. Lett.* **2011**, *504*, 71.
(215) Xia, T.; Otto, J. W.; Dutta, T.; Murowchick, J.; Caruso, A. N.; et al. *J. Mater. Res.* **2013**, *28*, 326.
(216) Li, G. H.; Gray, K. A. *Chem. Phys.* **2007**, *339*, 173.
(217) Zhao, Y.; Pan, F.; Li, H.; Zhao, D.; et al. *J. Phys. Chem. C* **2013**, *117*, 21718.
(218) Somorjai, G. A.; Bratlie, K. M.; Montano, M. O.; Park, J. Y. *J. Phys. Chem. B* **2006**, *110*, 20014.
(219) Tilocca, A.; Selloni, A. *J. Chem. Phys.* **2003**, *119*, 7445.
(220) Tilocca, A.; Selloni, A. *Langmuir* **2004**, *20*, 8379.
(221) Tilocca, A.; Selloni, A. *J. Phys. Chem. B* **2004**, *108*, 4743.
(222) Gong, X. Q.; Selloni, A.; Batzill, M.; Diebold, U. *Nat. Mater.* **2006**, *5*, 665.
(223) Scanlon, D. O.; Dunnill, C. W.; Buckeridge, J.; Shevlin, S. A.; Logsdail, A. J.; et al. *Nat. Mater.* **2013**, *12*, 798.
(224) Kavan, L.; Gratzel, M.; Gilbert, S. E.; Klemenz, C.; Scheel, H. J. *J. Am. Chem. Soc.* **1996**, *118*, 6716.
(225) Kawahara, T.; Konishi, Y.; Tada, H.; Tohge, N.; Nishii, J.; et al. *Angew. Chem., Int. Ed.* **2002**, *41*, 2811.
(226) Miyagi, T.; Kamei, M.; Mitsuhashi, T.; Ishigaki, T.; Yamazaki, A. *Chem. Phys. Lett.* **2004**, *390*, 399.
(227) Nakajima, H.; Mori, T.; Shen, Q.; Toyoda, T. *Chem. Phys. Lett.* **2005**, *409*, 81.
(228) Xiong, G.; Shao, R.; Droubay, T. C.; Joly, A. G.; Beck, K. M.; et al. *Adv. Funct. Mater.* **2007**, *17*, 2133.
(229) Xia, T.; Li, N.; Zhang, Y. L.; Kruger, M. B.; Murowchick, J.; et al. *ACS Appl. Mater. Interfaces* **2013**, *5*, 9883.
(230) Li, W.-K.; Hu, P.; Lu, G.; Gong, X.-Q. *J. Mol. Model.* **2014**, *20*, 2215.
(231) Majumder, S.; Paramanik, D.; Solanki, V.; Bag, B. P.; Varma, S. *Appl. Phys. Lett.* **2011**, *98*, 053105.
(232) Rahman, M.; MacElroy, J. M. D.; Dowling, D. P. *J. Nanosci. Nanotechnol.* **2011**, *11*, 8642.
(233) Kaur, K.; Singh, C. V. *Energy Procedia* **2012**, *29*, 291.
(234) Harris, L. A.; Schumacher, R. *J. Electrochem. Soc.* **1980**, *127*, 1186.
(235) Chen, Y. X.; Wei, Z. B.; Chen, Y. X.; Lin, H. X.; Hong, Z. P.; et al. *J. Mol. Catal.* **1983**, *21*, 275.
(236) Okamoto, K.; Yamamoto, Y.; Tanaka, H.; Tanaka, M.; Itaya, A. *Bull. Chem. Soc. Jpn.* **1985**, *58*, 2015.
(237) Heller, A.; Degani, Y.; Johnson, D. W.; Gallagher, P. K. *J. Phys. Chem.* **1987**, *91*, 5987.
(238) Khader, M. M.; Kheiri, F. M. N.; Elanadouli, B. E.; Ateya, B. G. *J. Phys. Chem.* **1993**, *97*, 6074.
(239) Qin, D. Y.; Chang, W. D.; Chen, Y.; Zhou, J. L.; Chen, Y. Q.; et al. *J. Catal.* **1993**, *142*, 719.
(240) Rekoske, J. E.; Barteau, M. A. *J. Phys. Chem. B* **1997**, *101*, 1113.
(241) Haerudin, H.; Bertel, S.; Kramer, R. *J. Chem. Soc., Faraday Trans.* **1998**, *94*, 1481.
(242) Liu, H.; Ma, H. T.; Li, X. Z.; Li, W. Z.; Wu, M.; et al. *Chemosphere* **2003**, *50*, 39.
(243) Chen, X.; Liu, L.; Liu, Z.; Marcus, M. A.; Wang, W.-C.; et al. *Sci. Rep.* **2013**, *3*, 1510.
(244) Xia, T.; Chen, X. *J. Mater. Chem. A* **2013**, *1*, 2983.
(245) Hu, Y. H. *Angew. Chem., Int. Ed.* **2012**, *51*, 12410.
(246) Wang, G.; Wang, H.; Ling, Y.; Tang, Y.; Yang, X.; et al. *Nano Lett.* **2011**, *11*, 3026.
(247) Zheng, Z.; Huang, B.; Lu, J.; Wang, Z.; Qin, X.; et al. *Chem. Commun.* **2012**, *48*, 5733.
(248) Wang, W.; Ni, Y.; Lu, C.; Xu, Z. *RSC Adv.* **2012**, *2*, 8286.
(249) Wang, Z.; Yang, C.; Lin, T.; Yin, H.; Chen, P.; et al. *Adv. Funct. Mater.* **2013**, *23*, 5444.
(250) Leshuk, T.; Linley, S.; Gu, F. *Can. J. Chem. Eng.* **2013**, *91*, 799.
(251) Leshuk, T.; Parviz, R.; Everett, P.; Krishnakumar, H.; Varin, R. A.; et al. *ACS Appl. Mater. Interfaces* **2013**, *5*, 1892.
(252) Danon, A.; Bhattacharyya, K.; Vijayan, B. K.; Lu, J.; Sauter, D. J.; et al. *ACS Catal.* **2012**, *2*, 45.
(253) Yu, X.; Kim, B.; Kim, Y. K. *ACS Catal.* **2013**, *3*, 2479.
(254) Lu, H. Q.; Zhao, B. B.; Pan, R. L.; Yao, J. F.; et al. *RSC Adv.* **2014**, *4*, 1128.
(255) Wang, W.; Lu, C.-H.; Ni, Y.-R.; Song, J.-B.; et al. *Catal. Commun.* **2012**, *22*, 19.

(256) Li, H.; Chen, Z. H.; Tsang, C. K.; Li, Z.; et al. *J. Mater. Chem. A* **2014**, *2*, 229.
(257) Zheng, L. X.; Cheng, H.; Liang, F. X.; Shu, S. W.; et al. *J. Phys. Chem. C* **2012**, *116*, 5509.
(258) Xu, C.; Song, Y.; Lu, L. F.; Cheng, C. W.; et al. *Nanoscale Res. Lett.* **2013**, *8*, 391.
(259) Buha, J. *J. Phys. D: Appl. Phys.* **2012**, *45*, 385305.
(260) Hoang, S.; Berglund, S. P.; Hahn, N. T.; Bard, A. J.; Mullins, C. B. *J. Am. Chem. Soc.* **2012**, *134*, 3659.
(261) Pan, H.; Zhang, Y.-W.; Shenoy, V. B.; Gao, H. *J. Phys. Chem. C* **2011**, *115*, 12224.
(262) Sodergren, S.; Siegbahn, H.; Rensmo, H.; Lindstrom, H.; Hagfeldt, A.; et al. *J. Phys. Chem. B* **1997**, *101*, 3087.
(263) Henningsson, A.; Rensmo, H.; Sandell, A.; Siegbahn, H.; Sodergren, S.; et al. *J. Chem. Phys.* **2003**, *118*, 5607.
(264) Howard, C. J.; Sabine, T. M.; Dickson, F. *Acta Crystallogr., Sect. B: Struct. Sci.* **1991**, *47*, 462.
(265) Tielens, F.; Calatayud, M.; Beltran, A.; Minot, C.; Andres, J. *J. Electroanal. Chem.* **2005**, *581*, 216.
(266) Lunell, S.; Stashans, A.; Ojamae, L.; Lindstrom, H.; Hagfeldt, A. *J. Am. Chem. Soc.* **1997**, *119*, 7374.
(267) Cava, R. J.; Murphy, D. W.; Zahurak, S.; Santoro, A.; Roth, R. S. *J. Solid State Chem.* **1984**, *53*, 64.
(268) Sudant, G.; Baudrin, E.; Larcher, D.; Tarascon, J. M. *J. Mater. Chem.* **2005**, *15*, 1263.
(269) van de Krol, R.; Goossens, A.; Meulenkamp, E. A. *J. Electrochem. Soc.* **1999**, *146*, 3150.
(270) Wagemaker, M.; Kentgens, A. P. M.; Mulder, F. M. *Nature* **2002**, *418*, 397.
(271) Wagemaker, M.; van de Krol, R.; Kentgens, A. P. M.; van Well, A. A.; Mulder, F. M. *J. Am. Chem. Soc.* **2001**, *123*, 11454.
(272) Wagemaker, M.; Borghols, W. J. H.; Mulder, F. M. *J. Am. Chem. Soc.* **2007**, *129*, 4323.
(273) Kavan, L.; Kalbac, M.; Zukalova, M.; Exnar, I.; Lorenzen, V.; et al. *Chem. Mater.* **2004**, *16*, 477.
(274) Kim, J.; Cho, J. *J. Electrochem. Soc.* **2007**, *154*, A542.
(275) Shin, J.-Y.; Joo, J. H.; Samuelis, D.; Maier, J. *Chem. Mater.* **2012**, *24*, 543.
(276) Lu, Z.; Yip, C.-T.; Wang, L.; Huang, H.; Zhou, L. *ChemPlusChem.* **2012**, *77*, 991.
(277) Li, G.; Zhang, Z.; Peng, H.; Chen, K. *RSC Adv.* **2013**, *3*, 11507.
(278) Shen, L.; Uchaker, E.; Zhang, X.; Cao, G. *Adv. Mater.* **2012**, *24*, 6502.
(279) Myung, S. T.; Kikuchi, M.; Yoon, C. S.; Yashiro, H.; et al. *Energy Environ. Sci.* **2013**, *6*, 2609.
(280) Yan, Y.; Hao, B.; Wang, D.; Chen, G.; et al. *J. Mater. Chem. A* **2013**, *1*, 14507.
(281) Lu, X.; Wang, G.; Zhai, T.; Yu, M.; Gan, J.; et al. *Nano Lett.* **2012**, *12*, 1690.
(282) Zhang, C.; Yu, H.; Li, Y.; Gao, Y.; Zhao, Y.; et al. *ChemSusChem* **2013**, *6*, 659.
(283) Zhu, W.-D.; Wang, C.-W.; Chen, J.-B.; Li, D.-S.; Zhou, F.; Zhang, H.-L. *Nanotechnology* **2012**, *23*, 455204.
(284) Zhao, D. L.; Li, X.; Shen, Z. M. *Compos. Sci. Technol.* **2008**, *68*, 2902.
(285) Yusoff, A. N.; Abdullah, M. H. *J. Magn. Magn. Mater.* **2004**, *269*, 271.
(286) Feng, Y. B.; Qiu, T.; Shen, C. Y.; Li, X. Y. *IEEE Trans. Magn.* **2006**, *42*, 363.
(287) Peng, C. H.; Wang, H. W.; Kan, S. W.; Shen, M. Z.; Wei, Y. M.; et al. *J. Magn. Magn. Mater.* **2004**, *284*, 113.
(288) Bowler, N. *IEEE Trans. Dielectr. Electr. Insul.* **2006**, *13*, 703.
(289) Deng, L. J.; Han, M. G. *Appl. Phys. Lett.* **2007**, *91*, 023119.
(290) Qing, Y. C.; Zhou, W. C.; Luo, F.; Zhu, D. M. *J. Magn. Magn. Mater.* **2009**, *321*, 25.
(291) Fan, Z. J.; Luo, G. H.; Zhang, Z. F.; Zhou, L.; Wei, F. *Mater. Sci. Eng., B* **2006**, *132*, 85.
(292) Petrov, V. M.; Gagulin, V. V. *Inorg. Mater.* **2001**, *37*, 93.
(293) Von Hippel, A. R. *Dielectric materials and applications*; Artech House: Boston, MA, 1995.
(294) Yu, P. Y.; M, C. *Fundamentals of Semiconductors: Physics and Materials Properties.*; Springer: Berlin, 2001.
(295) Xia, T.; Zhang, C.; Oyler, N. A.; Chen, X. *Adv. Mater.* **2013**, *25*, 6905.
(296) Soohoo, R. F. *Microwave magnetics*; Harper & Row Publishers: New York, 1985.
(297) Xia, T.; Zhang, C.; Oyler, N. A.; Chen, X. *J. Phys. Chem. C.* Submitted for publication.
(298) Naldoni, A.; Allieta, M.; Santangelo, S.; Marelli, M.; Fabbri, F.; et al. *J. Am. Chem. Soc.* **2012**, *134*, 7600.
(299) Jiang, X.; Zhang, Y.; Jiang, J.; Rong, Y.; Wang, Y.; et al. *J. Phys. Chem. C* **2012**, *116*, 22619.
(300) Wang, Z.; Yang, C.; Lin, T.; Yin, H.; et al. *Energy Environ. Sci.* **2013**, *6*, 3007.
(301) Onishi, Y. *Bull. Chem. Soc. Jpn.* **1971**, *44*, 912.
(302) Li, S.; Qiu, J.; Ling, M.; Peng, F.; et al. *ACS Appl. Mater. Interfaces* **2013**, *5*, 11129.
(303) Pesci, F. M.; Wang, G. M.; Klug, D. R.; Li, Y.; Cowan, A. J. *J. Phys. Chem. C* **2013**, *117*, 25837.
(304) Lu, J. B.; Dai, Y.; Jin, H.; Huang, B. B. *Phys. Chem. Chem. Phys.* **2011**, *13*, 18063.
(305) Gray, T. J.; McCain, C. C.; Masse, N. G. *J. Phys. Chem.* **1959**, *63*, 472.
(306) Chester, P. F. *J. Appl. Phys.* **1961**, *32*, 2233.
(307) Shannon, R. D. *J. Appl. Phys.* **1964**, *35*, 3414.
(308) Purcell, T.; Weeks, R. A. *J. Chem. Phys.* **1971**, *54*, 2800.
(309) Cho, E.; Han, S.; Ahn, H.-S.; Lee, K.-R.; Kim, S. K.; et al. *Phys. Rev. B* **2006**, *73*, 193202.
(310) Bartholo, R.; Frankl, D. R. *Phys. Rev.* **1969**, *187*, 828.
(311) Cronemeyer, D. C. *Phys. Rev.* **1959**, *113*, 1222.
(312) Becker, J. H.; Hosler, W. R. *Phys. Rev.* **1965**, *137*, 1872.
(313) Yagi, E.; Hasiguti, R. R.; Aono, M. *Phys. Rev. B* **1996**, *54*, 7945.
(314) Hasiguti, R. R.; Yagi, E. *Phys. Rev. B* **1994**, *49*, 7251.
(315) Sekiya, T.; Yagisawa, T.; Kamiya, N.; Das Mulmi, D.; Kurita, S.; et al. *J. Phys. Soc. Jpn.* **2004**, *73*, 703.
(316) Na-Phattalung, S.; Smith, M. F.; Kim, K.; Du, M. H.; Wei, S. H.; et al. *Phys. Rev. B* **2006**, *73*, 125205.
(317) Yu, N. C.; Halley, J. W. *Phys. Rev. B* **1995**, *51*, 4768.
(318) He, J.; Sinnott, S. B. *J. Am. Ceram. Soc.* **2005**, *88*, 737.
(319) Di Valentin, C.; Pacchioni, G.; Selloni, A. *Phys. Rev. Lett.* **2006**, *97*, 166803.
(320) Finazzi, E.; Di Valentin, C.; Pacchioni, G. *J. Phys. Chem. C* **2009**, *113*, 3382.
(321) Janotti, A.; Varley, J. B.; Rinke, P.; Umezawa, N.; Kresse, G.; et al. *Phys. Rev. B* **2010**, *81*, 085212.